

1 Revision 2

2

3 Chemical fingerprints and residence times of olivine in the 1959 Kilauea Iki eruption, Hawaii:
4 insights into picrite formation

5

6

7 Richard W. Bradshaw^{a,b}

8 Adam J. R. Kent^a

9 Frank J. Tepley III^a

10

11

12

13 ^aCollege of Earth, Ocean, and Atmospheric Sciences

14 Oregon State University

15 Corvallis, OR 97331

16 USA

17 ^bNew address: Department of Earth and Environmental Sciences

18 Vanderbilt University

19 Nashville, TN 37240

20 USA

21

22

23

24

Abstract

25

26

27

28

29

30

31

32

33

34

35

36

37

38

39

40

41

42

43

44

45

46

Olivine-rich mafic volcanic rocks (picrites) are a common and important part of ocean island and flood basalt volcanism. Despite their primitive bulk compositions (high MgO, FeO, Mg# and low SiO₂), olivine-rich magmas are typically interpreted as the result of addition of olivine from cumulate zones into more evolved basaltic liquids (MgO ≤ ~8 wt%). There are commonly two texturally distinct olivine populations in picrites: type 1 grains with planar dislocation (kink) bands, subgrains or undulose extinction; and type 2 grains that lack these optical textures. Type 1 olivine is similar in texture to olivine from tectonized ultramafic rocks, suggesting that these textures result from plastic deformation, likely within cumulate zones. However, recently it has been proposed that type 1 olivine could also result from growth phenomena or crystal-crystal collisions. In the Kilauea Iki picrite samples used in this study, type 1 grains make up only 10–20% of the modal olivine, however they make up 30–65% of the total olivine by volume due to their large size. Therefore, type 1 grains make a large contribution to the overall composition of Kilauea Iki picrites. A combination of textural (optical defects, crystal size distributions and minor element zoning) and geochemical analyses (trace element concentrations, and diffusion of minor elements) suggests that type 1 and type 2 olivine grains have experienced distinctly different petrological histories and that they are antecrysts and autocrysts, respectively. Differences between type 1 and type 2 olivine are evident in the abundances of slow diffusing trace elements (Al, P, Ti, V), which are likely inherited from their distinct parent magmas. Type 1 and type 2 grains also define different slopes in crystal size distributions, and constraints from diffusion of P and Cr suggest that type 1 grains have longer magmatic residence times than type 2 grains. Type 1 grains likely derive from deformed cumulates within the plumbing system of Kilauea volcano, and our work supports the hypothesis

47 that picrites from Kilauea Iki are formed by accumulation of antecrystic olivine in more evolved
48 basaltic liquid. Our work further supports models that type 1 olivine textures are formed during
49 plastic deformation within cumulate zones and are not the result of growth phenomena. Our
50 methods can be applied to other olivine-rich volcanic rocks to test the cumulate model for the
51 formation of type 1 olivine textures, which are relatively common in picritic and related rocks
52 from other settings.

53 **Keywords:** Kilauea Iki, olivine, picrite, diffusion, crystal size distribution, olivine
54 cumulate

55 **Introduction**

56 The compositions of mafic volcanic rocks from all tectonic settings provide key
57 information for understanding the origin and evolution of the Earth's mantle, and place important
58 constraints on the conditions and processes of mantle melting and the nature of mantle sources
59 (e.g., White 1985; Zindler and Hart 1986; Anderson and Brown 1993; Graham et al. 1998;
60 Révillon et al. 1999; Class and Goldstein 2005; Herzberg et al. 2007; Putirka et al. 2007; White
61 2010; Herzberg 2011; Poland et al. 2014). However, as most mafic magmas also experience
62 modification during transit and storage within the crust, the processes that work to alter the
63 magma composition during transport and crustal residence must also be understood and
64 corrected for where necessary (e.g., Herzberg 2011). In many cases the most mafic (high MgO,
65 Mg#, Ni) rocks in a given suite of lavas are selected as the magma compositions that are the least
66 modified from those in equilibrium with their mantle source. However, many volcanic rocks that
67 meet these primitive chemical characteristics are olivine-rich (e.g., picrites), and although some
68 olivine-rich, picritic rocks are interpreted to represent primary melts from the mantle whose
69 crystallized olivine remains entrained in the host liquid (Francis 1985), most picrites likely result

70 from the addition of olivine to a more evolved basaltic liquid (e.g., Murata and Richter 1966b;
71 Helz 1987; Albarede and Tamagnan 1988; Clague and Denlinger 1994; Garcia 1996; Révillon et
72 al. 1999; Thomson and Maclennan 2013). In this case much of the olivine present within a picrite
73 did not directly crystallize from the silicate liquid in which they are erupted, but are derived from
74 crustal cumulate zones or other sources (Francis 1985; Albarede and Tamagnan 1988; Clague
75 and Denlinger 1994; Baker et al. 1996; Garcia 1996; Révillon et al. 1999; Sakyi et al. 2012).

76 In detail, olivine accumulated within picritic magmas may be from a number of different
77 sources. These include *autocrysts* (following the nomenclature of Miller et al. 2007) that are
78 derived directly from the liquid fraction of the magma, *xenocrysts* from conduit walls at deep
79 crustal or lithospheric mantle levels, or *antecrysts* derived from disruption of cumulates and
80 other olivine-rich zones within the volcano's plumbing system (e.g., Helz 1987). At Hawaii, and
81 many other ocean island and flood basalt provinces, olivine-rich lavas contain a significant
82 fraction of "deformed" (type 1) olivine grains that exhibit characteristic multiple planar
83 extinction boundaries (kink bands), undulose extinction, or subgrains (Francis 1985; Helz 1987;
84 Albarede and Tamagnan 1988; Garcia 1996; Révillon et al. 1999; Larsen and Pedersen 2000;
85 Natland 2003; Sakyi et al. 2012; Thomson and Maclennan 2013; Welsch et al. 2013; 2014). The
86 traditional interpretation of this texture is that olivine grains are deformed at high temperatures
87 (>1100 °C) while they are stored in dunite cumulate zones (Francis 1985; Albarede and
88 Tamagnan 1988; Clague and Denlinger 1994; Baker et al. 1996; Garcia 1996; Révillon et al.
89 1999; Sakyi et al. 2012), analogous to deformation of olivine during shearing in the upper mantle
90 (e.g., Hansen et al. 2014). At Hawaii, this deformation is thought to be due to both the seaward
91 motion of the south flank of Kilauea and down-rift flow of olivine-rich cumulates (Clague and
92 Denlinger 1994; Clague et al. 1995; Denlinger and Morgan 2014). Type 1 grains derived from

93 cumulates are thus interpreted as antecrysts, while type 2 grains are considered to be autocrysts
94 that crystallize directly from the host liquid (Francis 1985; Albarede and Tamagnan 1988;
95 Clague and Denlinger 1994; Baker et al. 1996; Garcia 1996; Révillon et al. 1999; Sakyi et al.
96 2012).

97 However, the interpretation that type 1 olivine derives from cumulate zones has also been
98 challenged. Natland (2003) interpreted type 1 olivine textures in picrites from Juan Fernandez as
99 the result of crystal-crystal and crystal-conduit wall collisions that occur during magma mixing.
100 Alternatively, Welsch et al. (2013; 2014) concluded that type 1 olivine grains from Piton de la
101 Fournaise and Hawaii form as a result of initial rapid, dendritic growth of crystals followed by a
102 period of slower growth and infilling (ripening). This could produce the type 1 textural features
103 due to lattice mismatches developed during the dendritic growth phase and accentuated during
104 the ripening phase (Welsch et al. 2013; 2014). Although these alternative models do not exclude
105 the storage of type 1 olivine in cumulate zones, with these alternate models, storage and
106 deformation in a cumulate is not required to form the observed defects. Thus, a correct
107 interpretation of the origin of these olivine textures has real implications for the petrogenesis of
108 picrite magmas.

109 Resolving this question requires a means to fingerprint olivine grains in picrites that are
110 derived from different sources to understand how they are formed and are incorporated into their
111 host magma. This has proven difficult because the olivine grains are likely derived from
112 crystallization of similar magmas and both type 1 and type 2 olivine grains typically overlap
113 substantially in major element composition (e.g., Baker et al. 1996; Garcia 1996; Révillon et al.
114 1999; Welsch et al. 2013). The divalent major elements and most abundant trace elements in
115 olivine (e.g., Fe, Mg, Ni) also diffuse rapidly in olivine, thus they are readily re-equilibrated

116 during storage at high temperatures (Chakraborty 2010), which could also explain their
117 similarities. Olivine in mafic magmas commonly have geochemically homogeneous cores (not in
118 equilibrium with the host liquid) with narrow zoned rims, suggesting equilibration during
119 extended crystal residence followed by late-stage growth and/or diffusive re-equilibration in the
120 final, carrier magma (e.g., Helz 1987; Garcia 1996; Révillon et al. 1999; Salaün et al. 2010;
121 Thomson and Maclennan 2013). In contrast to rapidly diffusing major elements, slow diffusing
122 trace elements have been shown to record differences between separate olivine populations (e.g.,
123 Neave et al., 2018), and assuming equilibrium partitioning during growth, have the potential to
124 distinguish the petrogenesis of type 1 and type 2 olivine.

125 In this contribution, we utilize both geochemical (olivine trace element concentrations
126 and distributions) and textural information (deformation textures, zoning patterns and crystal size
127 distributions), to explore the sources of olivine in picrites from Kilauea Iki, Hawaii, and test the
128 validity of using textures alone to fingerprint olivine in mafic volcanic rocks. Differences in
129 crystal size distributions (CSD), trace element compositions and constraints from trace element
130 diffusion suggest that the type 1 olivine population is derived from a distinctly different source
131 and has a longer magmatic residence time than type 2 olivine.

132 **Geologic Setting**

133 Kilauea Iki crater is located east of the Kilauea Caldera on the Big Island of Hawaii. The
134 summit eruption of Kilauea Iki lasted from November 14 through December 20, 1959, and
135 consisted of 17 phases of fire fountaining, that partially filled the Kilauea Iki crater (Richter et al.
136 1970). The 1959 eruption is unique for Kilauea summit eruptions in that it produced high
137 fountains, involved abundant picritic lavas, and erupted lavas contained significant amounts of
138 type 1 olivine (Helz 1987; Garcia et al. 2003). The modal abundance of olivine in the erupted

139 lavas is also correlated with the eruption intensity (high fountaining events), which led to the
140 interpretation that the picritic nature of the lavas is due to the incorporation of olivine crystals
141 from deeper in the system into a volatile rich magma (Murata and Richter 1966a; 1966b; Helz
142 1987). The magma erupted at Kilauea Iki in 1959 is thought to have formed from mixing of a
143 primitive, mantle-derived magma (1959E) with a more evolved, shallowly-stored magma
144 (1959W; Wright 1973; Helz 1987).

145 Olivine is the dominant phenocryst phase (~4 to 30 modal%) present in Kilauea Iki lavas,
146 with minor plagioclase and clinopyroxene present only in the first and the last eruptive phases
147 (Richter and Murata 1966). In general, olivine core compositions are not in Fe/Mg equilibrium
148 with the dominant melts from this eruption (Helz et al. 2014). On the basis of textures, Helz
149 (1987) identified five populations of olivine in Kilauea Iki lavas: (1) blocky grains that contain
150 deformation features (kink-bands or subgrains), (2) euhedral to skeletal grains that are free of
151 deformation features, (3) rounded grains without deformation features, (4) rare, small conchoidal
152 fragments of grains, and (5) rare grains containing abundant sulfide inclusions. Helz (1987)
153 concluded that the class 1 (type 1, herein) olivine are antecrysts derived from the conduit wall in
154 the lower crust, class 2 grains are sourced from the shallow stored magma, and class 5 grains
155 were sourced from deep (but not as deep as class 1) in the plumbing system. Class 3 grains were
156 rounded and class 4 grains were fractured during mixing of the two thermally disparate magmas
157 (Helz 1987). Helz (1987) concluded that both the class 1 grains, and the sulfide-bearing grains
158 were derived from cumulates.

159 **Samples and Methods**

160 Five samples that were collected during the 1959 eruption of Kilauea Iki by USGS
161 scientists were obtained from the collection of the Department of Mineral Sciences, National

162 Museum of Natural History for this study. These samples were all collected from the rising lava
163 lake during the ongoing eruption and do not represent pumice samples. One additional scoria
164 sample was collected from the surface along the Devastation Trail in 2009. All samples were
165 prepared as polished thin sections.

166 Electron microprobe analyses of olivine were performed on a Cameca SX-100 at Oregon
167 State University. X-ray element maps were performed on selected olivine grains to map the
168 distribution of P, Al, and Cr in olivine following the techniques outlined by Milman-Barris et al.
169 (2008). This was accomplished using a focused $\sim 1 \mu\text{m}$ beam diameter, with an accelerating
170 voltage of 15 keV and a beam current of 400 nA. Dwell times for each pixel were between 75
171 and 200 ms and the spacing between pixels was between 2 and 5 μm . Images were exported as
172 16 bit TIFF files to preserve the x-ray intensities. To obtain higher resolution images and
173 increase the signal to noise ratio, while keeping analysis time within reasonable limits, elements
174 were analyzed on multiple spectrometers, and images were combined later using MATLAB and
175 ImageJ (Schneider et al. 2012). Aluminum was analyzed on two spectrometers (one TAP and
176 one LTAP crystal). Phosphorus was analyzed on either three spectrometers (one LPET and two
177 PET crystals), or on one spectrometer with the LPET crystal, with Cr analyzed on the other two
178 spectrometers with PET crystals. Analysis times were between 2 and 17 hours depending on the
179 size of the area of interest and the dwell time and pixel spacing.

180 Trace elements were analyzed by laser ablation using a Photon Machines Analyte G2 193
181 nm ArF excimer laser coupled with a Thermo Scientific Xseries2 Quadrupole inductively
182 coupled plasma mass spectrometer (ICP-MS). Olivine was analyzed using an 85 μm diameter
183 spot, at a pulse rate of 10 hz. Sample traverses were done as rim-to-rim line scans, with a scan
184 speed of 15 $\mu\text{m/s}$. Care was taken to avoid obvious melt and spinel inclusions; however, some

185 contamination is evident in several analyses and the affected portions of those transects were
186 removed during post analysis processing. Reference glass standard GSE-1G (analyzed every 6-8
187 unknowns) was used for calibration, natural glass standards BHVO-2G and BCR-2G as
188 secondary standards, and ^{29}Si was used as an internal standard. Data were processed using
189 standard calibration techniques (Longerich et al. 1996) to calculate concentrations for individual
190 time slices. Each data point is an average of five time slices, which is similar to the method of
191 Ruprecht and Plank (2013). Each data point represents an analytical area of approximately 85 by
192 120 μm and an analysis depth of $\sim 5 \mu\text{m}$. Uncertainties for each analysis were calculated by
193 propagating uncertainties in repeat measurements of the calibration standard in each session with
194 uncertainty in the measured normalized ratio for each set of time slices. Typical uncertainties for
195 these analyses are (1s): $<5\%$ for Mg, Al, Fe; $<10\%$ for Na, Ca, Sc, V, Mn, Co, Ni, Zn; $<20\%$ for
196 Li, Ti, Cr, Cu, Ga, Y, Zr, Mo, Ba, Ce, Dy, Er, Yb; $<30\%$ for P, Ge, and $<40\%$ for B. The
197 forsterite (Fo) content of analyzed olivine grains was estimated from the laser ablation data using
198 measured Fe/Si ratios. The estimated error in Fo is $\pm 0.95 \text{ mol}\%$ (RMSE) based on comparison
199 with electron microprobe analyses on the same locations on select grains. Laser ablation analyses
200 were also compared to the electron microprobe for Hawaiian and Snake River Plain olivine
201 (Bradshaw 2012) to assess the accuracy of this technique. The percent difference in composition
202 of select elements between the two techniques were calculated, and they agree well, but with
203 some systematic bias. The laser ablation results are higher for Mg (5%), Mn (30%), Fe (20%)
204 and Ni (10%) and lower for Ca (35%).

205 Electron backscatter diffraction (EBSD) analysis was done in the Linus Pauling Science
206 Center at Oregon State University using an FEI Quanta dual beam scanning electron microscope
207 equipped with an EDAX EBSD detector. Analyses were done using an accelerating voltage of 15

208 kV, current of 0.85 or 1.7 nA (adjusted to reduce charging of the sample). Samples were tilted to
209 an angle of 70° with a typical working distance between 12 and 14 mm. Samples were lightly
210 carbon coated to reduce sample charging.

211 Crystal size distributions were measured by outlining individual crystals in Adobe
212 Illustrator using high resolution scans of thin sections and verified by visual inspection using a
213 petrographic microscope. Type 1 and type 2 grains were outlined in different layers to allow a
214 comparison of their size characteristics. Individual crystals in glomerocrysts were measured
215 separately by visual inspection using a petrographic microscope. We measured 120 to 230
216 olivine grains in each of the five thin sections (Table 1). Outlined crystal intersections were
217 imported into ImageJ (Schneider et al. 2012) to calculate the area, orientation, length and width
218 of a best-fit ellipse. CSDslice (Morgan and Jerram 2006) was used to estimate the overall crystal
219 shape (short:intermediate:long dimensions) based on the 2D intersection data. There were too
220 few crystals in the individual samples to produce robust CSDs, so the combined CSD for all
221 samples was used. The best fit shape parameter from all crystals of 1.0:1.0:1.4 was calculated
222 using CSDslice (Morgan and Jerram 2006). These data were input into CSD Corrections 1.4
223 (Higgins 2000) to correct the 2D intersection data to 3D crystal size distributions on a vesicle-
224 free basis. For input into CSD Corrections, we specified the rock fabric as massive and estimated
225 the roundness to be 0.5, the same value estimated by Vinet and Higgins (2010; 2011) for Kilauea
226 olivine, including grains from the Kilauea Iki lava lake. As we focus on the pre-eruptive storage
227 conditions of these lavas, only grains larger than about 0.1 mm were outlined, and our
228 interpretations are based on grains larger than ~0.2 mm.

229 **Results and Discussion**

230 **Olivine Textures**

231 We have identified the same five textural classes identified by Helz (1987) in our sample
232 set, but we focus on the two major types, type 1 (class 1 of Helz) and type 2 grains (classes 2 and
233 3 of Helz). Due to analytical reasons (small size and abundant inclusions), and their rarity, class
234 4 and 5 grains are not included in this study. Type 1 grains are typically blocky and commonly
235 contain embayments, which we interpret as evidence of resorption (Figure 1), which is most
236 evident along the boundaries between kink bands. Type 1 grains are present in all samples, with
237 a modal proportion of 12 to 22% of the total olivine crystals (Table 1). Although there are fewer
238 type 1 crystals in our samples, they are larger than type 2 crystals and represent ~30 to 65% of
239 the crystal content by volume (Table 1), and therefore have a large effect on the bulk
240 composition of picrites. Type 2 grains (Helz 1987) are typically euhedral and are the most
241 common crystals in these samples (Table 1).

242 Type 1 and type 2 crystals were identified optically, which due to crystal size and also
243 sectioning effects may result in misidentification of type 1 grains. Vinet et al. (2011) used in situ
244 x-ray diffraction to study the deformation of single olivine crystals from Mauna Ulu and Kilauea
245 Iki, Hawaii, and were able to identify type 1 grains as small as 0.15 mm. In the optical methods
246 applied here, we did not identify type 1 grains smaller than 0.28 mm, therefore some small, type
247 1 grains may have been misidentified. Type 1 grains can also be misidentified due to their
248 orientation as optical defects are not visible in olivine grains whose a-axes are parallel to the
249 plane of the thin section (Boudier 1991). Type 1 olivine textures were successfully identified
250 optically in grains with their a-axes oriented as close as 5 degrees from the plane of the section,
251 as determined by EBSD. Therefore, assuming all crystals are randomly oriented (verified by
252 EBSD analysis; Table 2), only about 6% of type 1 grains would be misidentified due to their
253 orientation within the plane of the thin section. In the work of Vinet et al. (2011) only ~6% of

254 type 2 grains identified optically (3 out of 54 total grains) were determined to be type 1 grains
255 using in situ x-ray diffraction, which may suggest that those grains were also misidentified
256 optically due to their orientation.

257 **Trace Element Variations in Olivine**

258 Intra-grain trace element variations are evident in LA-ICP-MS transects across both type
259 1 and type 2 olivine and also in X-ray element maps of minor elements (P, Al and Cr; Figures 2,
260 3; Supplemental Material). These within-grain variations in both olivine types are most evident
261 in P (c.f., Milman-Barris et al. 2008; Welsch et al. 2013; 2014; Xing et al., 2017), but minor
262 zoning in Al, Ti, V, Cr, Cu, Sr, Y, and Zr is also present in some grains. Zoning of P is common
263 in both type 1 and type 2 olivine and is also observed in most P X-ray element maps (Table 3,
264 Figures 2, 3). The variation in P and equivalent zoning in Al and Cr, as observed in element
265 maps, is likely the result of kinetic effects during rapid crystal growth (Milman-Barris et al.
266 2008; Grant and Kohn 2013; Welsch et al. 2013; 2014).

267 To compare the compositions of type 1 and type 2 grains, regions of transects with
268 elevated P contents (compared to the remainder of the transect) were removed to eliminate any
269 kinetic effects from analysis of rapid growth zones (Milman-Barris et al. 2008; Grant and Kohn
270 2013; Welsch et al. 2013; 2014). To accomplish this, the laser ablation transects were compared
271 to their associated P maps to identify and remove the locations along the transects affected by
272 high P zones (Figures 2, 3). For grains without P maps only the portions of the profiles with the
273 lowest P in grains with clear P zonation were included in this analysis. By means of comparison
274 we also performed the comparison between the two olivine types without removing zones of
275 elevated P.

276 When comparing type 1 and type 2 grains, data are plotted as cumulative distribution
277 functions (CDF), which can show differences, or similarities between populations even where
278 there is considerable overlap in the data (Figure 4). Two-sample Kolmogorov-Smirnov tests
279 (which quantifies the difference between two CDFs, Press et al. 1992) were performed to assess
280 whether type 1 and type 2 grains are sampled from the same population (Table 4), using a
281 significance level of 95% ($\alpha = 0.05$). To avoid overweighting of larger crystals (which contain
282 more individual analyses) the Kolmogorov-Smirnov tests were performed using the median
283 concentrations of the laser transects for each grain (both including and excluding high P zones).

284 Type 1 and type 2 grains, from Hawaii and elsewhere, have previously been recognized
285 as indistinguishable in major element compositions (e.g., Helz 1987; Baker et al. 1996; Garcia
286 1996; Welsch et al. 2013). This is also evident here as the p-value for the Kolmogorov-Smirnov
287 test is high for Fo ($p = 0.56$), and other major and minor elements ($p > 0.26$ for Mg, Ca, and Ni)
288 in Kilauea Iki olivine (Table 4), meaning that the null hypothesis that the major elements from
289 type 1 and type 2 grains sample the same population cannot be rejected at our selected level of
290 confidence (95%). However, we can reject this null hypothesis for Al, P, Ti and V ($p < 0.05$;
291 Table 4) in type 1 and type 2 grains, suggesting these two types of olivine contain distinctly
292 different abundances of these elements and thus sample different populations. When high P
293 zones are not removed, the same slow diffusing elements (Al, P, Ti and V) still have
294 significantly low p-values ($p < 0.01$; Table 4).

295 This apparent discrepancy between Fe, Mg, Ca, and Ni (and other divalent cations)
296 compared to Al, P, Ti, and V, where the former sample a single population and the latter two
297 different populations can be best explained by the different diffusion rates among these elements.
298 The major elements and many divalent trace elements (Mg, Mn, Fe, Co, Ni) in olivine have

299 relatively rapid diffusion rates ($> 10^{-16} \text{ m}^2/\text{s}$ at 1300 °C; Chakraborty 2010; Cherniak and Liang
300 2014; Watson et al. 2015); therefore their original compositions will be modified by diffusive re-
301 equilibration more readily than slower diffusing elements such as Al, Cr, P and V, which are
302 more likely to preserve their original compositional information.

303 The differences evident in chemical composition in the slow diffusing trace elements also
304 suggest that these two textural populations of olivine derive from different composition magmas,
305 and/or formed under pressures and temperature conditions sufficient to affect element
306 partitioning into olivine. However, it is also difficult to relate these differences directly to
307 magmatic compositions. Higher overall Al and Ti in type 1 olivine (Figure 4) might suggest that
308 type 1 olivine formed from melts more enriched in incompatible elements, but P contents in type
309 1 crystals are lower. In addition, there has also likely been some intra-grain diffusive
310 redistribution of these slow diffusing elements, as evidenced by the relaxation or elimination of
311 Al zoning (see below). Within-grain diffusion acted to remove elemental zoning produced during
312 crystal formation (e.g. Millman-Barris et al., 2008), but if this occurred while the grains were in
313 equilibrium with their original liquids, or within a cumulate pile (Thomson and MacLennan,
314 2011) this can still maintain overall composition differences. We also note that some other slow
315 diffusing elements (e.g. Y, REEs) do not appear to sample separate populations. Although this
316 might reflect the possibility that no differences exist between these two olivine populations with
317 respect to these elements, we note that these are also elements present at lower abundance in
318 olivine, and thus also have higher analytical uncertainties, which makes resolving different
319 populations more difficult (Figure 5).

320 Although both olivine textural types overlap completely in major element composition,
321 Helz (1987) reports various patterns of zoning in Fo content in Kilauea Iki olivine, with olivine

322 from classes (types) 1 and 2 exhibiting both normal (core compositions $> \text{Fo}_{86}$) and reverse
323 zoning (cores $< \text{Fo}_{86}$). This was attributed to olivine being derived from different depths beneath
324 the summit and varying degrees of equilibration (Helz, 1987). We observe a slightly larger range
325 in Fo content than Helz (1987; Fo_{85-88}), with 6 grains having a median Fo content < 84 mole %
326 (three from each textural type), and a total range from Fo_{82-89} , and note the presence of some
327 reversely zoned crystals. However, in our samples there are no obvious Fo-delineated
328 populations, and the trace element abundances are similar between high ($> 86\%$) and low Fo ($<$
329 86%) olivine. What does emerge from our data is the trace element differences between type 1
330 and type 2 olivine, suggesting that these populations had distinct histories regardless of apparent
331 storage depth.

332 **Crystal Size Distributions**

333 Crystal size distributions of Kilauea Iki olivine grains were determined to further
334 understand the processes that control the formation of these two olivine populations. The CSD
335 data are shown in Figure 6, where type 1 and type 2 grains are plotted separately. There are too
336 few grains from individual samples to plot robust CSDs, so we focus on the overall results from
337 all samples combined. Vinet and Higgins (2011) also performed CSD analyses for Kilauea Iki,
338 mainly focusing on lava lake samples, but they did analyze three scoria samples collected from
339 the surface. They identified two main olivine populations (based on two linear segments of
340 curved CSDs), a smaller crystal population (G2a), consisting of mostly type 2 olivine, and a
341 larger crystal population (G2b), with a significant proportion of type 1 grains (Vinet and Higgins
342 2011). Mangan (1990) measured CSDs for type 2 grains in 8 of the eruptive phases of the 1959
343 eruption and combined them to improve precision. Vinet and Higgins (2011) recalculated the
344 original crystal size measurements of Mangan (1990) using the shape parameters from olivine

345 from the lava lake and area to volume estimates from CSD Corrections (Higgins 2000). In this
346 study, in order to examine the differences between type 1 and type 2 crystals in more detail we
347 explicitly separate them to investigate the contribution of each olivine texture to the overall CSD.

348 The type 1-only and type 2-only curves in Figure 6 are both approximately linear, with
349 the type 1-only curve having a shallower slope and extending to larger crystals than the type 2-
350 only curve. The type 1-only curve does not extend to the smallest crystal sizes, which could be
351 the result of physical processes during crystal growth and storage that cause differences in CSD
352 shape (Higgins 2006a) but could also be the result of misidentification, as small, type 1 grains
353 are more difficult to identify optically. Although this type of misidentification would also have
354 an effect on the slope of the CSD, we note that along with the evidence presented above, there is
355 not a substantial downturn of the type 1 CSD at the smallest crystal sizes, suggesting that the
356 misidentification of small, type 1 grains is minimal. Any type 1 grains that were misidentified
357 from being oriented with the a-axis parallel to the section should affect both the type 1 and type 2
358 CSDs equally as these grains should be misidentified equally across all grain sizes because the
359 crystals are randomly oriented (Table 2). Therefore, the effect of misidentification due to crystal
360 orientation would only shift the position of the curves, with no change in slope. Our CSD results
361 are similar to the previous studies of Mangan (1990) and Vinet and Higgins (2011). The type 1
362 CSD slope and intercept are similar to the G2b population of Vinet and Higgins (2011), which
363 contains significant type 1 crystals (Table 5). The type 2 crystals are similar to the G2a
364 population of Vinet and Higgins (2011) and the type 1-only CSD of Mangan (1990) (Table 5).
365 As with previous studies (Helz 1987; Garcia 1996; Vinet and Higgins 2010; Vinet et al. 2011;
366 Vinet and Higgins 2011; Sakyi et al. 2012), we also find that type 1 grains extend to larger

367 crystal sizes than type 2 grains. The largest type 1 grain identified in our samples is 5.56 mm,
368 and the largest type 2 grain is 1.95 mm (long axis).

369 The differences in the shapes of these CSD curves also suggest that there are significant
370 differences in the crystallization and storage histories of these two different textural crystal
371 populations. The shallow slope of the type 1-grain CSD curve (Figure 6; Table 5), could be the
372 result of extended growth (residence) time of type 1 olivine, higher growth rates, textural
373 coarsening, accumulation of olivine or a combination of these (Higgins 2006a). Faster growth
374 rates for the type 1 olivine population could explain the shallower slope and larger crystals
375 compared with the type 2 olivine population. In the dendritic growth model of Welsch et al.
376 (2013) it would be expected that crystals with P zoning would grow large due to a rapid initial
377 growth phase. However, this is at odds with the observation that both type 1 and type 2 olivine
378 are zoned in P, but only the type 1 grains are large, which argues against a single process
379 producing both olivine textures, unless the formation of defects require even more rapid growth.
380 If P-enrichment occurs in a similar way regardless of growth rate – above a certain threshold
381 growth rate – then defects could form in *very* rapidly grown olivine and could produce larger
382 type 1 grains with similar zoning patterns to type 2 grains; however, this is unlikely because as
383 we show below, zoning of P, Al, and Cr should be affected by growth rates, therefore we would
384 expect to see a difference in the concentrations of these elements and their zoning patterns. An
385 alternative explanation for the difference in crystal size between these two olivine populations is
386 textural coarsening. Vinet and Higgins (2010; 2011) also observed a shallower slope for several
387 CSDs that included type 1 grains in Mauna Ulu and Kilauea Iki lava lake samples, which they
388 interpreted as the result of textural coarsening. Textural coarsening (Ostwald Ripening) occurs
389 when larger grains grow at the expense of smaller grains (Marsh 1988; Higgins 2006a; 2011),

390 and is a process that could readily occur during residence within a cumulate zone (Vinet and
391 Higgins 2010; Higgins 2011). The steeper slope and lack of a downturn at the smallest sizes for
392 the type 2 crystals suggest that such coarsening did not affect this population. Although we agree
393 with Vinet and Higgins (2010; 2011) that coarsening has affected the crystals in the Kilauea Iki
394 samples, we suggest it only affected the type 1 grains in the surface samples. The recognition of
395 textural coarsening of type 1 grains potentially implies longer residence than type 2 grains, as
396 additional time would be needed for the type 1 grains to coarsen, assuming the two populations
397 had similar initial crystallization histories (as evidenced by P zoning). Several type 1 grains also
398 have resorption textures, which suggests that they experienced disequilibrium conditions that
399 resulted in some reduction in size prior to eruption. However, this minor amount of resorption
400 could occur late in the development of the crystals, after significant coarsening, resulting in the
401 overall large sizes of type 1 crystals.

402 The Kilauea Iki eruption is well known to be a product of magma mixing (Wright 1973;
403 Helz 1987; Garcia et al. 2003; Helz et al. 2014; Poland et al. 2014; Wright and Klein 2014),
404 which may also have affected the shape of the CSD. Mixing of two magmas with different CSD
405 slopes and intercepts will produce a kinked CSD with two linear segments, representing the
406 slopes of the CSDs for the original magmas (e.g., Higgins 2006a; Salisbury et al. 2008; Kent et
407 al. 2010). The total crystal CSD (both type 1 and type 2 grains) for all samples (Figure 6) has
408 two nearly linear segments (also observed by Vinet and Higgins, 2011) that resembles a mixing
409 situation; however, the larger crystal size population is made up mostly of type 1 grains.
410 Therefore, the curvature of the total CSD is primarily the result of incorporation of type 1
411 olivine. Although two distinct segments are not evident in the single population CSDs, the type 2
412 olivine population exhibits a slight curve, as indicated by the lower value of the goodness of fit

413 (Q) parameter (Table 5; Higgins 2006b). This may indicate that more subtle effects of magma
414 mixing are present, possibly representing the mixing of the 1959E and 1959W endmembers of
415 Helz (1987), which mixed two similar (but not identical) populations of type 2 grains.

416 **Minor element zoning**

417 The Kilauea Iki samples used in this study have many grains with zoning in the minor
418 elements P, Al and Cr (Figures 2, 3, Supplemental Material), as has been observed in olivine from
419 Hawaii and a number of other systems (e.g., Milman-Barris et al. 2008; Sakyi et al. 2012;
420 Welsch et al. 2013; 2014). Zoning of these elements in Kilauea Iki olivine is evident in electron
421 microprobe x-ray maps (Figures 2, 3). Most of the grains imaged by this technique show zoning
422 in P, and several of those grains also show corresponding zoning in Al and Cr (Table 3), which
423 has also been observed in natural and experimentally grown olivine (e.g., Milman-Barris et al.
424 2008). The zoning in these elements is mostly independent of any zoning in major elements (Fo)
425 and in many cases is not obviously related to the final crystal shape or to the presence of planar
426 defects (Figure 3). Crystals commonly have hopper-shaped, high-P cores that can be either sharp
427 or diffuse. Most crystals, whether or not they are zoned in the cores, have one or more thin, sharp
428 zones at or near the rim that match the final shape of the crystals, suggesting they are late-stage
429 growth zones. One hopper-shaped groundmass crystal exhibits zoning that matches the crystal
430 shape, and one highly resorbed grain has oscillatory zoning that is disrupted by dissolution
431 surfaces (Figure 2). Zoning in P is generally not disrupted by crystal edges, however, there are a
432 few examples of zoning that is truncated by dissolution surfaces (~11/66 grains; Figure 7).
433 Identifying truncated P zones is somewhat ambiguous because P zonation is typically
434 discontinuous within crystals (see images herein and in Milman-Barris, 2008; Welsch et al.,
435 2013; 2014). Also, in the cases where P zoning is truncated, there is typically a narrow, low-P

436 area between the high P zone and the crystal edge, indicating that some crystallization has
437 occurred subsequent to dissolution. Of the crystals with identified truncations in P zoning, 8 are
438 type 1 and 3 are type 2 crystals. This truncation of P zoning shows that these crystals
439 experienced disequilibrium conditions sometime before eruption and could be the result of their
440 incorporation into magmas of different composition, either by disruption of a cumulate or during
441 magma mixing.

442 Although the electron probe x-ray mapping technique used to identify minor element
443 zoning is time consuming, we have imaged a sufficiently large number of crystals to investigate
444 whether there is a relationship between the presence of P and Cr zoning in the two olivine
445 populations. Both type 1 and type 2 grains commonly exhibit zoning in P, with 24/25 type 1
446 grains and 39/44 type 2 grains showing P zoning (Table 3). Using the binomial distribution, it is
447 possible to evaluate whether these proportions are significantly different from one another. The
448 binary distribution is used to calculate the probability of obtaining one of two outcomes when the
449 same population is sampled randomly and independently (e.g., Taylor 1997). If we take the
450 probability of a crystal having P zoning as equal to the combined proportions of crystals
451 observed with P zoning (e.g., 63/69 or $p = 0.91$) then the probability of obtaining the observed
452 proportion of type 1 and type 2 crystals with P zoning is 23 and 16% respectively, and at 95%
453 confidence ($\alpha = 0.05$) we cannot reject the null hypothesis that the proportions of olivine with P-
454 zoning are the same in type 1 and type 2 crystals. In contrast, the proportions of crystals with
455 observed Cr zoning evident are much lower for type 1 crystals (4/21) than for type 2 (12/21).
456 Applying the same methodology and assuming the proportion of Cr zoning in all crystals is the
457 combined proportions (16/42, $p = 0.38$) the probability that either type 1 or type 2 crystals show
458 Cr zoning in the observed proportions is $\ll 5\%$, allowing us to reject the null hypothesis that

459 there is no difference in the proportion of crystals with Cr zoning between type 1 and type 2
460 grains. If we instead use the observed proportions of Cr zoned crystals in type 1 and type 2
461 crystals separately to set the p value then probabilities that Cr zoning in type 1 olivine occur in
462 the same proportions as in type 2 grains, and vice versa, are even lower ($\ll 1\%$), again allowing
463 us to reject the null hypothesis. Applying this methodology to Al, the probability that crystals
464 show Al zoning in the observed proportions is 12% for type 1 and 10% for type 2 olivine, thus
465 the null hypothesis cannot be rejected at the 95% confidence level. However, if we use the
466 observed proportions of Al zoning in type 1 and type 2 crystals separately to set the p value, then
467 the probabilities that Al zoning occurs in the same proportions are 2% for type 1 grains and type
468 2 grains and the null hypothesis can be rejected.

469 Although there are differences in the number of crystals that exhibit zoning in P, Al, and
470 Cr between type 1 and type 2 grains, it is likely that the incorporation of these three elements
471 into olivine is a linked process. Phosphorus may be incorporated in olivine at elevated
472 concentrations during periods of rapid crystal growth by both equilibrium partitioning of
473 elevated P contents in enriched boundary layers and also by non-equilibrium solute trapping—
474 where rapid olivine growth “runs over” these P enriched boundary layers (Milman-Barris et al.
475 2008; Grant and Kohn 2013; Welsch et al. 2014). To explain the similar zoning of P, Al, and Cr
476 in natural and experimentally grown olivine, Milman-Barris et al (2008) concluded that P is
477 incorporated at high concentrations with a coupled substitution with Al and Cr. Grant and Kohn
478 (2013) did not observe a correlation between P with Al in their equilibrium experiments, but
479 speculated that under non-equilibrium conditions (solute trapping), P may partition with a
480 growth rate-dependent coupled substitution with Al and Cr. Alternatively, Watson et al. (2015)
481 propose that the growth enrichment model (Watson and Liang 1995), which invokes differential

482 partitioning behavior of the surface layer of a growing crystal with the interior and intra-
483 crystalline diffusion better explains the enrichment of P in olivine. Regardless of the exact
484 partitioning behavior of these elements, evidence suggests that Al and Cr are likely incorporated
485 in olivine along with P. In olivine, Al and Cr also diffuse more rapidly than P (Ito and Ganguly
486 2006; Milman-Barris et al. 2008; Watson et al. 2015), and Milman-Barris et al (2008) argued that
487 Al and Cr zoning profiles in the natural phenocrysts are erased during extended storage at high
488 temperatures while P zoning was preserved, which agrees with our observations.

489 To further establish that Al and Cr are incorporated in olivine in higher concentrations
490 where elevated P is observed we have applied a boundary layer model (Smith et al. 1955; Baker
491 2008). This approach models the enrichment of incompatible elements at the boundary of a
492 growing crystal, taking into account the crystal growth rate, the olivine-liquid partition
493 coefficient, and the diffusivity of the element in the melt. Our goal is to understand the
494 conditions that lead to P-rich boundary layers during olivine crystallization in Kilauea Iki and
495 other basaltic magmas, and to assess whether we can reasonably expect Al and Cr to be
496 consistently enriched in these zones by this same process. Watson et al (2015) performed similar
497 models for P, and here we also model Al and Cr to understand their behavior. Welsch et al.
498 (2013) predicted that the incorporation of P in olivine at high concentrations occurs during
499 periods of rapid, dendritic growth, which occurs at growth rates of $\sim 10^{-6}$ m/s and that subsequent
500 ripening, of the crystal occurs at a slower growth rate of $\sim 10^{-9}$ m/s. We therefore modeled the
501 boundary layer of a crystal after 10 μm of growth using this range of expected growth rates,
502 similar to the method of Watson et al. (2015).

503 Boundary layer models for P, Al and Cr (Figure 8), show that these elements are enriched
504 at the boundary of the growing olivine at high growth rates (10^{-6} m/s). Our results for P match

505 the results of the same modeling by Watson et al. (2015), and show enrichments factors of >4
506 and >1.5 at growth rates of 10^{-6} and 10^{-7} m/s, respectively (Figure 8). At the highest growth rate,
507 Al and Cr are also enriched by factors of 1.4 and ~ 1.2 , respectively (Figure 8). The observed
508 enrichment factors from our laser ablation data for P ranges from 1.5 to 11 (median of 2.5),
509 which agree with the highest growth rates in the boundary layer models. The growth enrichment
510 model (GEM), proposed by Watson et al. (2015) to explain P zoning in olivine, may also
511 produce enrichments of Al and Cr in olivine. However, the partitioning behavior for these
512 elements in the surface layer of olivine is not well constrained, so we did not attempt to model
513 this here. Importantly for our purpose, our modeling suggests that P, Al, and Cr are co-enriched
514 at the olivine-liquid boundary during rapid crystal growth, and that instances where enrichment
515 of P occurs within olivine during rapid growth without enrichment of Al and Cr are unlikely. It is
516 also important to note that although diffusion may erase the Al and Cr zonation, there are
517 observed, significant differences in the absolute concentrations of Al (and P, Ti, and V) between
518 type 1 and type 2 olivine (Table 4) that are unrelated to mineral zoning. This suggests that
519 although Al is incorporated at higher concentrations along with P and diffusive re-equilibration
520 of Al may erase the initial zoning, these elements also record the last equilibration conditions of
521 these crystals. Also, the concentration of P is higher in type 2 crystals than type 1 crystals (with
522 and without excluding the P-rich zones from the analysis), which is the opposite of what would
523 be expected for the dendritic growth model if elevated P is indicative of type 1 textures.

524 Zoning of trace elements in olivine provides a means to constrain the timescales of
525 crystal residence at magmatic temperatures in the Kilauea system. Although diffusion of divalent
526 cations in olivine is frequently used to infer the timescales of eruptive processes (e.g., Nakamura
527 1995; Coombs et al. 2000; Pan and Batiza 2002; Costa and Chakraborty 2004; Kahl et al. 2011;

528 2013; Marti et al. 2013; Ruprecht and Plank 2013; Longpre et al. 2014), we are more interested
529 in the longer timescales of crystal residence and thus focus on the slower diffusing elements, Cr
530 and P.

531 To effectively estimate diffusion timescales, appropriate diffusion coefficients are
532 needed. Ito and Ganguly (2006) measured diffusion coefficients for Cr in olivine and found that
533 it is highly anisotropic with little dependence on oxygen fugacity, at least from the wustite-iron
534 buffer to two log units above this buffer (Ito and Ganguly 2006). The oxygen fugacity of these
535 experiments was lower than what is reasonable for Hawaiian magmas; however, the calculated
536 diffusivities were the same over two orders of magnitude change in fO_2 (Ito and Ganguly 2006).
537 Therefore, it is likely that this diffusion coefficient is also appropriate for our samples. Diffusion
538 of Cr is anisotropic (Ito and Ganguly 2006), therefore the diffusion coefficient for Cr along the
539 measured transect was calculated using the equation

$$540 \quad D_{\text{traverse}} = D_a(\cos\alpha)^2 + D_b(\cos\beta)^2 + D_c(\cos\gamma)^2 \quad (1)$$

541 where D_a , D_b , D_c are the Cr diffusion coefficients along the a, b, and c-axes respectively, and α ,
542 β , γ are the angles between the traverse and the a, b, and c-axes respectively as determined by
543 EBSD (Costa et al. 2008). Watson et al. (2015) report a diffusion coefficient for P in olivine, and
544 determined that diffusion is isotropic and not dependent on fO_2 (experiments performed at NNO
545 and WM buffers). Watson et al. (2015) also confirm that P diffuses at a slower rate than Cr, as
546 had been previously inferred (Ito and Ganguly 2006; Milman-Barris et al. 2008). To date, the
547 diffusivity of Al in olivine has not been determined, therefore Al is not modeled here. We
548 evaluate the uncertainties in the diffusion modeling using a Monte Carlo approach to take into
549 account the uncertainties in the diffusion coefficients and temperature (Ito and Ganguly 2006;
550 Putirka 2008; Watson et al. 2015) and conclude that the uncertainties for these two diffusion

551 coefficients are less than a factor of 2.5. The spatial resolution of the geochemical analysis is
552 another source of uncertainty for short diffusion timescales and was evaluated using the method
553 of Bradshaw and Kent (2017). Using the spatial resolutions (step size in individual x-ray element
554 maps) and diffusivities for individual crystals, we calculate the shortest timescales that can be
555 accurately calculated between 0.4 and 4.8 days for Cr diffusion and between 6 and 30 days for P
556 diffusion.

557 Diffusion is strongly temperature dependent, and as the temperature at which diffusion
558 occurs is not well constrained, this is often a large source of uncertainty in estimated timescales
559 (Costa et al. 2008). Many of the olivine grains in this study are inferred to be antecrystic,
560 therefore the temperature at which they formed could not be estimated using the observed whole
561 rock or glass compositions. Therefore, we calculated the equilibrium liquid from the composition
562 of individual olivine grains and equilibration temperatures using the MgO-liquid thermometer of
563 Helz and Thornber (1987) for Kilauea Iki and has an uncertainty of ± 10 °C. The equilibrium
564 liquid Mg# ($\text{Mg}/(\text{Fe}+\text{Mg})$) was estimated using a K_D of 0.28 and a $\text{Fe}^{3+}/(\text{Fe}^{2+} + \text{Fe}^{3+})$ ratio of
565 0.17 (Helz et al. 2017). The MgO content of the equilibrium liquid was then estimated using the
566 observed trend of MgO and Mg# for Kilauean lavas (compilation taken from the GeoRoc
567 database: georoc.mpch-mainz.gwdg.de/). Results are given in Table 6 with an average from all
568 grains of 1182 ± 21 °C (one standard deviation, 1s) for both type 2 and type 1 grains. We used
569 the temperatures estimated from individual crystals using a $\text{FeO}/\text{MgO } K_D^{\text{Olivine/melt}}$ of 0.28 for
570 diffusion modeling. For comparison, the average temperature estimates using other published K_D
571 values range from 1251 ± 30 °C using a K_D of 0.30 (Roeder and Emslie 1970), to 1277 ± 32 °C
572 using a K_D of 0.33 (Putirka 2014), to 1286 ± 32 °C using a K_D of 0.34 (Matzen et al. 2011).
573 Using the temperatures derived from these higher K_D values would result in shorter absolute

574 diffusion timescales. For example, using a K_D of 0.34 results in estimated residence times that
575 are shorter by approximately a factor of 2.

576 Compositional gradients for diffusion modeling of P and Cr were extracted from the
577 electron microprobe x-ray element maps, which give better spatial resolution than LA-ICP-MS
578 analysis, and allows us to see the zoning in two dimensions to select transects that are normal to
579 zoning (Figure 9). Profiles of distance versus counts (as greyscale intensity) were taken directly
580 from the 16 bit x-ray element maps using ImageJ (Schneider et al. 2012). Diffusion modeling
581 was performed using an analytical solution of the diffusion equation for diffusion of an initial
582 compositional step function, assuming isothermal diffusion, after Crank (1975)

$$583 \quad C = C_0 + \frac{(C_1 - C_0)}{2} \left[\operatorname{erfc} \left(\frac{x}{2\sqrt{Dt}} \right) \right] \quad (2)$$

584 where C is the concentration of the modeled profile, C_0 and C_1 are the initial concentrations on
585 either side of the step function interface at time zero, D is diffusivity (m^2/s), t is the diffusion
586 time (seconds), and x is distance (m) along the compositional gradient relative to the center of
587 the step function. The assumption of initial step function geometry results in maximum
588 timescales for the case where zoning has not been completely erased. To estimate the initial
589 zoning profiles for grains with P zoning but without observed Cr zoning, profiles with sharp P
590 zoning were selected, and the range of initial Cr intensity was derived from analyses of olivine
591 grains with similar P variation that also had Cr zoning. The calculated timescales for the case
592 where Cr zoning has been erased are minimum estimates as more time could have elapsed after
593 the initial zoning was erased (Figure 9).

594 For type 1 grains, the modeled diffusion timescales are between 10 days and 43 years for
595 Cr diffusion and between < 33 and 238 days for P diffusion (Table 7, Figure 10, Supplemental
596 Material). For type 2 grains, the timescales are between < 2 and 82 days for Cr diffusion, and <

597 22 and 127 days for P diffusion (Table 7, Figure 10). Several grains produced timescales that are
598 below the lowest accurate timescale estimate and cannot be more accurately constrained with our
599 spatial resolution (Table 7; Bradshaw and Kent, 2017); these are depicted as arrows in Figure 10.
600 There is some discrepancy in the timescales estimated for Cr and P diffusion in individual grains,
601 which is most evident in type 1 grains that do not have observed zoning in Cr (Table 7). We also
602 note that the choice of initial conditions for estimating the timescales needed to erase Cr zoning
603 have a relatively large effect on the calculated timescales. We chose the initial conditions based
604 on the Cr intensities in type 2 olivine grains with similar magnitudes of P zoning, however, if the
605 initial zoning of Cr was less pronounced, then the calculated timescales would be shorter.
606 Preliminary modeling of one such profile (Iki-Scoria-14E), suggests that for any case where Cr
607 zoning was initially present, it would take years to erase the Cr zoning.

608 An important observation is that most type 1 grains do not have equivalent Cr zoning
609 evident with P, whereas more of the type 2 grains do (Tables 2, 6), and as shown above, this
610 difference is statistically significant. Assuming there was initially Cr zoning present, long
611 residence times (years to decades) are thus needed to remove all indication of enriched Cr.
612 However, the timescale estimates from P for these same profiles are much lower and overlap
613 with P and Cr timescales from type 2 grains (Figure 10). This discrepancy may be because our
614 assumption that Cr zoning always accompanies P zoning in type 1 grains is not correct.
615 However, constraints from kinetic modeling and the presence of Cr zoning in similar type 2 (and
616 some type 1) grains suggest that type 1 olivine crystals did have initial Cr zoning. Type 1 and
617 type 2 grains have significantly different proportions of olivine with Cr zoning, suggesting that
618 there is some fundamental difference between these two olivine populations. Our data is more

642 **Summary of Observations and Interpretations**

643 There are several observations presented above, which need to be satisfied by any model
644 for the formation of Kilauea Iki (and other) picrites and their contained olivine.

- 645 • Presence of two distinct olivine populations based on optical characteristics: type
646 1 and type 2 grains (e.g., Helz 1987; Natland 2003; Welsch et al. 2013).
- 647 • The two olivine populations are geochemically distinct, most evident in slow
648 diffusing trace elements (P, Al, Ti, V), which likely reflects differences in source
649 magma compositions or formation and storage conditions.
- 650 • The two olivine populations have different CSD slopes (with the type 1-only
651 slope being shallower), and that the type 1 olivine grains may have experienced
652 textural coarsening.
- 653 • Residence time estimates, from Cr and P diffusion models suggest that the type 1
654 olivine grains have experienced a longer magmatic residence than the type 2
655 grains.

656 **Existing Models for Picrite Formation**

657 Central to any model for the assembly of picrites must address the origins of the two
658 textural and geochemical populations of olivine. The traditional model (Francis 1985; Albarede
659 and Tamagnan 1988; Clague and Denlinger 1994; Baker et al. 1996; Garcia 1996; Révillon et al.
660 1999; Sakyi et al. 2012) states that type 1 olivine is sourced from deforming cumulates beneath
661 the volcano, and type 2 olivine crystallizes from the host liquid. Recent models have suggested
662 that type 1 olivine textures may be the result of collisions (Natland 2003), or growth effects
663 (Welsch et al. 2013; 2014). In this section, we explore the existing models for the formation of

664 olivine, and test whether their predictions satisfy the observations for the origins of distinct
665 olivine populations.

666 Below, we focus on mechanisms that might produce type 1 and type 2 texture in
667 autocrystic or antecrystic olivine, rather than lithospheric olivine incorporated as xenocrysts. As
668 argued elsewhere (e.g., Larsen and Pedersen 2000), the low to moderate Ca contents and
669 presence of melt inclusions in both textural types argue against olivine derived directly from
670 mantle peridotite (Simkin and Smith 1970; Helz 1987; Garcia et al. 2007; Vinet and Higgins
671 2010; 2011). Low Ca content is consistent with these olivine grains crystallizing from magmas at
672 low pressure (e.g., Simkin and Smith 1970), and are not likely due to re-equilibration as it would
673 take hundreds of years for Ca to diffuse into the largest type 1 crystals (using diffusion
674 coefficients from Chakraborty, 2010).

675 **Non-cumulate models.** Non-cumulate models must account for the formation of type 1
676 olivine textures during growth and transport within a liquid. Natland (2003) suggests that olivine
677 grains experience non-hydrostatic stresses resulting from crystal-crystal or crystal-conduit wall
678 collisions during flow, which could cause type 1 olivine textures. However, Welsch et al. (2013)
679 noted that there is little evidence for collisions seen on the surfaces of type 1 olivine. The model
680 of Natland (2003) also does not account for the differences in the geochemistry we observe
681 between type 1 and type 2 olivine (assuming equilibrium partitioning) because, although it would
682 require two magmas with different olivine compositions and textures to mix, the collisions that
683 would produce deformation are thought to be enhanced during magma mixing, so olivine from
684 both magmas would have type 1 textures. The collisions suggested to produce deformation also
685 are predicted to fracture the grains to produce the conchoidal fragments recognized by Helz
686 (1987), but this fragmentation would cause a net decrease in the size of type 1 grains, which is

687 not consistent with crystal size observations. This model also does not explain the different
688 residence times of the two olivine populations. The two magmas that mixed during the Kilauea
689 Iki eruption were an older, shallow, stored magma (1959W) and a younger magma that bypassed
690 the summit reservoir (1959E) and intersected the stored magma (Wright 1973; Helz 1987;
691 Poland et al. 2014; Wright and Klein 2014). In this scenario, the olivine from the younger
692 ascending magma would be more likely to be deformed during its rapid ascent (Helz 1987) and
693 would produce two olivine populations with type 1 grains with *shorter* residence times and type
694 2 grains with *longer* residence times, the opposite of our modeling results.

695 The other alternative model is presented by Welsch et al. (2013; 2014) who suggest that
696 type 1 olivine grains are the result of a two-stage growth history, with initial rapid, dendritic
697 growth followed by slower growth and ripening of the crystals. In essence, as a crystal grows
698 rapidly, crystal “buds” grow dendritically from a single crystal, then during the slow-growth
699 phase those “buds” eventually grow into one another (Welsch et al. 2013). The resulting mosaic
700 of crystals would have an overall shape similar to euhedral olivine, but any lattice mismatches
701 among the different crystal “buds” would cause their boundaries to be misaligned and create type
702 1 olivine textures (Welsch et al. 2013), which would explain the first observation.

703 For the dendritic growth model of Welsch et al. (2013; 2014) to explain our other
704 observations, the chemical differences we observed require that the type 1 and type 2 grains were
705 sourced from separate magmas or that crystallization occurred at far-from-equilibrium conditions
706 that were different for type 1 and type 2 grains. In our samples, about the same proportion of
707 type 1 and type 2 olivine exhibit P zoning (Table 3), which is a major prediction of the dendritic
708 growth model for *type 1* grains (Welsch et al. 2013; 2014). Therefore, either the two-stage
709 growth predicted to produce type 1 olivine is not the cause of type 1 textures or the lattice

710 mismatches that produce these textures are rare. The rapid growth that enriches olivine in P,
711 would also enrich it in Al (and Ti, V, and Cr), therefore, we would expect type 1 olivine to have
712 higher overall P, Al, Ti, and V contents than type 2 olivine. However, we observe that P
713 concentrations are *lower*, and Al, Ti, and V are *higher* in type 1 grains than type 2 grains (Figure
714 4), which further suggests that zoning in P and Al is not correlated with defects in olivine.

715 The dendritic growth model of Welsch et al. (2013; 2014) also does not explain the
716 different textural features of type 1 and type 2 grains, such as the different CSD slopes, crystal
717 shapes, and crystal sizes. These textural differences could be explained if the different olivine
718 populations were sourced from separate magmas that mixed during the eruption. However, as
719 discussed above, both populations have P zoning and thus likely underwent similar growth
720 histories, and thus should have similar textures and sizes.

721 **Cumulate model.** A cumulate model best explains our observations for the assembly of
722 Kīlauea Iki and other lavas containing type 1 olivine. In this model type 1 textures in olivine are
723 formed by plastic deformation in a deforming olivine cumulate, which are later disrupted and
724 incorporated in unrelated ascending magmas (Helz 1987; Albarede and Tamagnan 1988; Clague
725 and Denlinger 1994; Garcia 1996; Garcia et al. 2007; Vinet and Higgins 2010). This explains the
726 presence of geochemically distinct populations of type 1 and type 2 olivine in the same magma,
727 with the type 1 grains being sourced from the disaggregated cumulate, and the type 2 grains from
728 the carrier magma(s). This process would also produce CSDs with different slopes and average
729 grain sizes for the type 1 and type 2 grains, as the type 1 grains would likely experience textural
730 coarsening during storage in the cumulate, whereas the CSD for the type 2 grains would only
731 record their crystallization history. Type 1 grains also show more evidence for dissolution and
732 fewer have euhedral shapes than type 2 grains, which is likely the consequence of partial

733 dissolution during the disruption of the cumulates. This dissolution appears to be a minor part of
734 the history of type 1 olivine, and it likely occurred after a significant amount of coarsening
735 occurred within the cumulate, thus preserving the large sizes of these crystals. This model also
736 explains how the type 1 population has a longer residence time than the type 2 population due to
737 extended storage in a cumulate.

738 Type 1 olivine from cumulate zones would be readily available as these cumulate zones
739 have been estimated to comprise 14 vol% of Hawaiian volcanoes (Clague and Denlinger 1994),
740 and have been imaged as zones of high seismic wave velocity beneath the summits and rift zones
741 of Hawaiian volcanoes (e.g., Okubo et al. 1997; Kauahikaua et al. 2000; Denlinger and Morgan
742 2014). The seaward flow of these dense cumulates, the same process interpreted to form
743 deformation textures in olivine, may also be the source of gravitational instability that leads to
744 large landslides that dissect these volcanoes (Clague and Denlinger 1994; Clague and Sherrod
745 2014; Denlinger and Morgan 2014).

746 A criticism of the deforming cumulate model is that some of the type 1 crystals have
747 euhedral outlines (Welsch et al. 2013; 2014). Welsch et al. (2013; 2014) argue that because some
748 type 1 grains have euhedral outlines, they could not have been plastically deformed, and
749 therefore type 1 olivine textures must be a primary growth feature. Overall, in Kilauea Iki
750 magmas, type 1 crystals with euhedral habits are less common than euhedral type 2 crystals. Of
751 the crystals analyzed in this study, <20% of type 1 crystals were classified as euhedral, whereas
752 60% of type 2 grains are euhedral. Type 1 grains may develop euhedral outlines during cooling
753 after disaggregation from a cumulate as shown in the melting experiments of Boudier (1991).
754 The experiments of Boudier (1991) produced euhedral crystal faces of deformed grains during
755 the relatively slow cooling (several minutes) after experimental melting of peridotite, which

756 allowed the olivine grains to obtain equilibrium where they were in contact with the liquid
757 produced during melting. Although euhedral forms are not produced during melting (e.g., Soulie
758 et al., 2017), the experiments of Boudier (1991) show that they may form relatively quickly
759 during the slower cooling obtained in that particular experimental setup, as opposed to the rapid
760 quenching in other experiments. This process observed during slowly-cooled melting
761 experiments, may be analogous to the processes involved in the disaggregation of a crystal-rich
762 cumulate as the crystals may achieve equilibrium with the surrounding intercumulus liquid
763 during cooling and could explain the ubiquity (yet low abundance of) euhedral crystals. The
764 euhedral, type 1 crystals in this study commonly contain thin, sharp P zones near to and parallel
765 with the crystal rims, suggesting late-stage rapid crystallization related to rim growth, which may
766 record the crystallization after disaggregation from a cumulate. Several crystals (8 type 1 and 3
767 type 2) also have evidence for P zoning truncation near resorption surfaces, suggesting they
768 experienced some dissolution, which may be the result of partial dissolution during disruption in
769 a cumulate. Boudier (1991) also showed that dissolution of olivine is more pronounced along
770 zones of weakness such as deformation boundaries, which may explain the common
771 embayments at the edges of type 1 grains (Figure 1), as opposed to them being dendritic crystal
772 buds as proposed by Welsch et al. (2013; 2014).

773 **Type 2 Olivine Source.** Type 2 olivine crystals likely have a less complicated history
774 than type 1 olivine. The most likely source for type 2 grains is from one or both of the magmas
775 that mixed to form the Kilauea Iki eruption. The type 2 grains are commonly euhedral, which has
776 been interpreted to mean that they crystallized, uninhibited in a melt (Helz 1987; Welsch et al.
777 2013), although euhedral crystals may also form during cooling after partial melting (e.g.,
778 Boudier 1991). The slight curvature of the type 2-only CSD (Table 5) suggests that there may be

779 two slightly different populations of type 2 grains. If this is the case it is likely to be the result of
780 mixing between the 1959E and 1959W endmember magmas as suggested by Wright (1973) and
781 Helz (1987). These magmas are both similar, and crystallize similar olivine grains, thus the
782 curvature on the CSD is small and we see no obvious compositional bimodality in the type 2
783 population, suggesting that any difference in minor element (P, Al, Cr, V) composition between
784 olivine from these two sources is smaller than differences between type 1 and type 2 olivine.

785

Implications

786 Our work suggests that type 1 and type 2 olivine in Kilauea Iki picrites require different
787 conditions for their formation. Type 1 and type 2 olivine likely experience similar initial growth
788 histories as evidenced by similar P zoning; however, type 1 grains require non-hydrostatic stress
789 to develop deformation textures. Type 1 olivine textures do not appear to result from growth
790 phenomena or subsequent crystal collisions. These results suggest that the type 1 grains in
791 Kilauea Iki magmas were sourced from an olivine-rich cumulate zone deeper in the plumbing
792 system, where prolonged crystal residence and plastic deformation occurs. These type 1 grains
793 were likely sampled by the ascending deep magma (1959E) during times of rapid ascent, as
794 evidenced from the high fountaining events. The type 2 grains are autocrysts sourced from both
795 the deep magma (1959E), and the older magma (1959W) stored beneath Kilauea Iki. Similar to
796 Kilauea Iki, many other volcanoes erupt picrites that contain both type 1 and type 2 olivine (e.g.,
797 Francis 1985; Albarede and Tamagnan 1988; Révillon et al. 1999) and may have experienced
798 similar processes in their formation.

799 Our methods can be applied to olivine-rich volcanic rocks from other locations to further
800 test the cumulate model for the formation of deformation textures in olivine. Our work shows the
801 value of combining an array of textural and geochemical observations in studying the origin of

802 olivine crystals in picritic magmas and emphasizes the important role of olivine-rich cumulate
803 zones in controlling the production of olivine-rich picritic magmas.

804 **Acknowledgements**

805 We thank Matt Loewen and Andy Ungerer for training and assistance with the laser
806 ablation ICP-MS analysis and Peter Eschbach and Teresa Sawyer for their training and
807 assistance with the SEM and EBSD analysis. We also thank Mike Garcia for discussions of
808 Hawaiian magmatism. Reviews by R. Helz, B. Welsch, and editorial handling and review by J.
809 Hammer substantially improved this manuscript. This work was supported by NSF grant EAR-
810 1425491 to AJRK and a GSA Graduate Student Research grant to RWB.

811

812

813

References

- 814 Albarede, F., and Tamagnan, V. (1988) Modelling the recent geochemical evolution of the Piton
815 de la Fournaise Volcano, Reunion Island, 1931-1986. *Journal of Petrology*, 29, 997–
816 1030.
- 817 Anderson, A.T.J., and Brown, G.G. (1993) CO₂ contents and formation pressures of some
818 Kilauean melt inclusions. *American Mineralogist*, 78, 794–803.
- 819 Baker, D.R. (2008) The fidelity of melt inclusions as records of melt composition. *Contributions*
820 *to Mineralogy and Petrology*, 156, 377–395.
- 821 Baker, D.R., Alves, S., and Stolper, E.M. (1996) Petrography and petrology of the Hawaii
822 Scientific Drilling Project lavas: Inferences from olivine phenocryst abundances and
823 compositions. *Journal of Geophysical Research*, 101, 11715–11727.
- 824 Beattie, P. (1993) Olivine-melt and orthopyroxene-melt equilibria. *Contributions to Mineralogy*
825 *and Petrology*, 115, 103–111.
- 826 Boudier, F. (1991) Olivine xenocrysts in picritic magmas. *Contributions to Mineralogy and*
827 *Petrology*, 109, 114–123.
- 828 Bradshaw, R.W., and Kent, A.J.R. (2017) The analytical limits of modeling short diffusion
829 timescales. *Chemical Geology*, <http://dx.doi.org/10.1016/j.chemgeo.2017.07.018>.
- 830 Chakraborty, S. (2010) Diffusion Coefficients in Olivine, Wadsleyite and Ringwoodite. *Reviews*
831 *in Mineralogy and Geochemistry*, 72, 603–639.
- 832 Cherniak, D.J., and Liang, Y. (2014) Titanium diffusion in olivine. *Geochimica et*
833 *Cosmochimica Acta*, 147, 43–57.
- 834 Clague, D.A., and Denlinger, R.P. (1994) Role of olivine cumulates in destabilizing the flanks of
835 Hawaiian volcanoes. *Bulletin of Volcanology*, 56, 425–434.

- 836 Clague, D.A., and Sherrod, D.R. (2014) Growth and Degradation of Hawaiian Volcanoes. U.S.
837 Geological Survey Professional Paper 1801, 97–146.
- 838 Clague, D.A., Moore, J.G., Dixon, J.E., and Friesen, W.B. (1995) Petrology of submarine lavas
839 from Kilauea's Puna Ridge, Hawaii. *Journal of Petrology*, 36, 299–349.
- 840 Class, C., and Goldstein, S.L. (2005) Evolution of helium isotopes in the Earth's mantle. *Nature*,
841 436, 1107–1112.
- 842 Coombs, M.L., Eichelberger, J.C., and Rutherford, M.J. (2000) Magma storage and mixing
843 conditions for the 1953–1974 eruptions of Southwest Trident volcano, Katmai National
844 Park, Alaska. *Contributions to Mineralogy and Petrology*, 140, 99–118.
- 845 Costa, F., and Chakraborty, S. (2004) Decadal time gaps between mafic intrusion and silicic
846 eruption obtained from chemical zoning patterns in olivine. *Earth and Planetary Science
847 Letters*, 227, 517–530.
- 848 Costa, F., Dohmen, R., and Chakraborty, S. (2008) Time Scales of Magmatic Processes from
849 Modeling the Zoning Patterns of Crystals. *Reviews in Mineralogy and Geochemistry*, 69,
850 545–594.
- 851 Crank, J. (1975) *The Mathematics of Diffusion: 2d Ed, 2nd ed.*, 1 p. Clarendon Press, London.
- 852 Denlinger, R.P., and Morgan, J.K. (2014) Instability of Hawaiian volcanoes. In *Characteristics of
853 Hawaiian Volcanoes* pp. 149–176. U.S. Geological Survey Professional Paper 1801.
- 854 Francis, D. (1985) The Baffin Bay lavas and the value of picrites as analogues of primary
855 magmas. *Contributions to Mineralogy and Petrology*, 89, 144–154.
- 856 Garcia, M.O. (1996) Petrography and olivine and glass chemistry of lavas from the Hawaii
857 Scientific Drilling Project. *Journal of Geophysical Research*, 101, 11701–11713.

- 858 Garcia, M.O., Haskins, E.H., Stolper, E.M., and Baker, M. (2007) Stratigraphy of the Hawai'i
859 Scientific Drilling Project core (HSDP2): Anatomy of a Hawaiian shield volcano.
860 Geochemistry Geophysics Geosystems, 8, Q02G20.
- 861 Garcia, M.O., Pietruszka, A.J., and Rhodes, J.M. (2003) A petrologic perspective of Kīlauea
862 volcano's summit magma reservoir. Journal of Petrology, 44, 2313–2339.
- 863 Graham, D.W., Larsen, L.M., Hanan, B.B., Storey, M., Pedersen, A.K., and Lupton, J.E. (1998)
864 Helium isotope composition of the early Iceland mantle plume inferred from the Tertiary
865 picrites of West Greenland. Earth and Planetary Science Letters, 160, 241–255.
- 866 Grant, T.B., and Kohn, S.C. (2013) Phosphorus partitioning between olivine and melt: An
867 experimental study in the system Mg_2SiO_4 - $Ca_2Al_2Si_2O_9$ - $NaAlSi_3O_8$ - $Mg_3(PO_4)_2$.
868 American Mineralogist, 98, 1860–1869.
- 869 Hansen, L.N., Zhao, Y.-H., Zimmerman, M.E., and Kohlstedt, D.L. (2014) Protracted fabric
870 evolution in olivine: Implications for the relationship among strain, crystallographic
871 fabric, and seismic anisotropy. Earth and Planetary Science Letters, 387, 157–168.
- 872 Helz, R., and Thornber, C.R. (1987) Geothermometry of Kilauea Iki lava lake, Hawaii. Bulletin
873 of Volcanology, 49, 651–668.
- 874 Helz, R.T. (1987) Diverse olivine types in lava of the 1959 eruption of Kilauea Volcano and
875 their bearing on eruption dynamics. USGS Professional Paper 1350, 1, 691–722.
- 876 Helz, R.T., Clague, D.A., Sisson, T.W., and Thornber, C.R. (2014) Petrologic insights into
877 basaltic volcanism at historically active hawaiian volcanoes. U.S. Geological Survey
878 Professional Paper 1801, 237–292.

- 879 Helz, R.T., Cottrell, E., Brounce, M.N., and Kelley, K.A. (2017) Olivine-melt relationships and
880 syneruptive redox variations in the 1959 eruption of K  lauea Volcano as revealed by
881 XANES. *Journal of Volcanology and Geothermal Research*, 333-334, 1–14.
- 882 Herzberg, C. (2011) Basalts as temperature probes of Earth's mantle. *Geology*, 39, 1179–1180.
- 883 Herzberg, C., Asimow, P.D., Arndt, N., Niu, Y., Leshner, C.M., Fitton, J.G., Cheadle, M.J., and
884 Saunders, A.D. (2007) Temperatures in ambient mantle and plumes: Constraints from
885 basalts, picrites, and komatiites. *Geochemistry Geophysics Geosystems*, 8, Q02006.
- 886 Higgins, M.D. (2000) Measurement of crystal size distributions. *American Mineralogist*, 85,
887 1105–1116.
- 888 Higgins, M.D. (2006a) Quantitative Textural Measurements in Igneous and Metamorphic
889 Petrology, 265 p. pp. 1–265. Cambridge University Press, Cambridge.
- 890 Higgins, M.D. (2006b) Verification of ideal semi-logarithmic, lognormal or fractal crystal size
891 distributions from 2D datasets. *Journal of Volcanology and Geothermal Research*, 154,
892 8–16.
- 893 Higgins, M.D. (2011) Textural coarsening in igneous rocks. *International Geology Review*, 53,
894 354–376.
- 895 Ito, M., and Ganguly, J. (2006) Diffusion kinetics of Cr in olivine and ⁵³Mn–⁵³Cr
896 thermochronology of early solar system objects. *Geochimica et Cosmochimica Acta*, 70,
897 799–809.
- 898 Kahl, M., Chakraborty, S., Costa, F., and Pompilio, M. (2011) Dynamic plumbing system
899 beneath volcanoes revealed by kinetic modeling, and the connection to monitoring data:
900 An example from Mt. Etna. *Earth and Planetary Science Letters*, 308, 11–22.

- 901 Kahl, M., Chakraborty, S., Costa, F., Pompilio, M., Liuzzo, M., and Viccaro, M. (2013)
902 Compositionally zoned crystals and real-time degassing data reveal changes in magma
903 transfer dynamics during the 2006 summit eruptive episodes of Mt. Etna. *Bulletin of*
904 *Volcanology*, 75, 692.
- 905 Kauahikaua, J., Hildenbrand, T., and Webring, M. (2000) Deep magmatic structures of Hawaiian
906 volcanoes, imaged by three-dimensional gravity models. *Geology*, 28, 883–886.
- 907 Kent, A.J.R., Darr, C., Koleszar, A.M., Salisbury, M.J., and Cooper, K.M. (2010) Preferential
908 eruption of andesitic magmas through recharge filtering. *Nature Geoscience*, 3, 631–636.
- 909 Larsen, L.M., and Pedersen, A.K. (2000) Processes in high-Mg, high-T Magmas: Evidence from
910 olivine, chromite and glass in Palaeogene picrites from West Greenland. *Journal of*
911 *Petrology*, 41, 1071–1098.
- 912 Longerich, H.P., Jackson, S.E., and Gunther, D. (1996) Laser ablation inductively coupled
913 plasma mass spectrometric transient signal data acquisition and analyte concentration
914 calculation. *Journal of Analytical Atomic Spectrometry*, 11, 899–904.
- 915 Longpre, M.A., Stix, J., Costa, F., Espinoza, E., and Munoz, A. (2014) Magmatic Processes and
916 Associated Timescales Leading to the January 1835 Eruption of Cosiguina Volcano,
917 Nicaragua. *Journal of Petrology*, 55, 1173–1201.
- 918 Mangan, M.T. (1990) Crystal size distribution systematics and the determination of magma
919 storage times: The 1959 eruption of Kilauea volcano, Hawaii. *Journal of Volcanology*
920 *and Geothermal Research*, 44, 295–302.
- 921 Marsh, B.D. (1988) Crystal size distribution (CSD) in rocks and the kinetics and dynamics of
922 crystallization 1. Theory. *Contributions to Mineralogy and Petrology*, 99, 277–291.

- 923 Marti, J., Castro, A., Rodriguez, C., Costa, F., Carrasquilla, S., Pedreira, R., and Bolos, X. (2013)
924 Correlation of Magma Evolution and Geophysical Monitoring during the 2011-2012 El
925 Hierro (Canary Islands) Submarine Eruption. *Journal of Petrology*, 54, 1349–1373.
- 926 Matzen, A.K., Baker, M.B., Beckett, J.R., and Stolper, E.M. (2011) Fe-Mg Partitioning between
927 Olivine and High-magnesian Melts and the Nature of Hawaiian Parental Liquids. *Journal*
928 *of Petrology*, 52, 1243–1263.
- 929 Miller, J.S., Matzel, J.E.P., Miller, C.F., Burgess, S.D., and Miller, R.B. (2007) Zircon growth
930 and recycling during the assembly of large, composite arc plutons. *Journal of*
931 *Volcanology and Geothermal Research*, 167, 282–299.
- 932 Milman-Barris, M.S., Beckett, J.R., Baker, M.B., Hofmann, A.E., Morgan, Z., Crowley, M.R.,
933 Vielzeuf, D., and Stolper, E. (2008) Zoning of phosphorus in igneous olivine.
934 *Contributions to Mineralogy and Petrology*, 155, 739–765.
- 935 Morgan, D.J., and Jerram, D.A. (2006) On estimating crystal shape for crystal size distribution
936 analysis. *Journal of Volcanology and Geothermal Research*, 154, 1–7.
- 937 Murata, K.J., and Richter, D.H. (1966a) Chemistry of the lavas of the 1959-60 eruption of
938 Kilauea volcano, Hawaii. *US Geological Survey Professional Paper*, 537-A, 1–26.
- 939 Murata, K.J., and Richter, D.H. (1966b) The settling of olivine in Kilauean magma as shown by
940 lavas of the 1959 eruption. *American Journal of Science*, 264, 194–203.
- 941 Nakamura, M. (1995) Residence time and crystallization history of nickeliferous olivine
942 phenocrysts from the northern Yatsugatake volcanoes, Central Japan: Application of a
943 growth and diffusion model in the system Mg-Fe-Ni. *Journal of Volcanology and*
944 *Geothermal Research*, 66, 81–100.

- 945 Natland, J.H. (2003) Capture of helium and other volatiles during the growth of olivine
946 phenocrysts in picritic basalts from the Juan Fernandez Islands. *Journal of Petrology*, 44,
947 421–456.
- 948 Neave, D.A., Shorttle, O., Oeser, M., Weyer, S., and Kobayashi, K. (2018) Mantle-derived trace
949 element variability in olivines and their melt inclusions. *Earth and Planetary Science*
950 *Letters*, 483, 90–104.
- 951 Okubo, P.G., Benz, H.M., and Chouet, B.A. (1997) Imaging the crustal magma sources beneath
952 Mauna Loa and Kilauea volcanoes, Hawaii. *Geology*, 25, 867–870.
- 953 Pan, Y., and Batiza, R. (2002) Mid-ocean ridge magma chamber processes: Constraints from
954 olivine zonation in lavas from the East Pacific Rise at 9°30'N and 10°30'N. *Journal of*
955 *Geophysical Research*, 107.
- 956 Poland, M.P., Miklius, A., and Montgomery-Brown, E.K. (2014) Magma supply, storage, and
957 transport at shield-stage Hawaiian volcanoes. U.S. Geological Survey Professional Paper
958 1801, 179–234.
- 959 Press, W.H., Teukolsky, S.A., Vetterling, W.T., and Flannery, B.P. (1992) *Numerical Recipes*,
960 2nd ed., 994 p. pp. 1–994. Cambridge University Press, New York.
- 961 Putirka, K.D. (2008) Thermometers and Barometers for Volcanic Systems. *Reviews in*
962 *Mineralogy and Geochemistry*, 69, 61–120.
- 963 Putirka, K.D. (2014) Fe-Mg exchange between olivine and liquid as a test of equilibrium:
964 Promises and pitfalls. *Geological Society of America Abstracts with Programs*, 46, 197.
- 965 Putirka, K.D., Perfit, M., Ryerson, F.J., and Jackson, M.G. (2007) Ambient and excess mantle
966 temperatures, olivine thermometry, and active vs. passive upwelling. *Chemical Geology*,
967 241, 177–206.

- 968 Révillon, S., Arndt, N.T., Hallot, E., Kerr, A.C., and Tarney, J. (1999) Petrogenesis of picrites
969 from the Caribbean Plateau and the North Atlantic magmatic province. *LITHOS*, 49, 1–
970 21.
- 971 Richter, D.H., and Murata, K.J. (1966) Petrography of the lavas of the 1959-60 eruption of
972 Kilauea volcano, Hawaii. US Geological Survey Professional Paper, 537-D, 1–18.
- 973 Richter, D.H., Eaton, J.P., Murata, K.J., Ault, W.U., and Krivoy, H.L. (1970) Chronological
974 narrative of the 1959-60 eruption of Kilauea Volcano, Hawaii. USGS Professional Paper,
975 537-E, 1–73.
- 976 Roeder, P.L., and Emslie, R. (1970) Olivine-liquid equilibrium. *Contributions to Mineralogy and*
977 *Petrology*, 29, 275–289.
- 978 Ruprecht, P., and Plank, T. (2013) Feeding andesitic eruptions with a high-speed connection
979 from the mantle. *Nature*, 500, 68–72.
- 980 Sakyi, P.A., Tanaka, R., Kobayashi, K., and Nakamura, E. (2012) Inherited Pb isotopic records
981 in olivine antecryst-hosted melt inclusions from Hawaiian lavas. *Geochimica et*
982 *Cosmochimica Acta*, 95, 169–195.
- 983 Salaün, A., Villemant, B., Semet, M.P., and Staudacher, T. (2010) Cannibalism of olivine-rich
984 cumulate xenoliths during the 1998 eruption of Piton de la Fournaise (La Réunion
985 hotspot): Implications for the generation of magma diversity. *Journal of Volcanology and*
986 *Geothermal Research*, 198, 187–204.
- 987 Salisbury, M.J., Bohron, W.A., Clynne, M.A., Ramos, F.C., and Hoskin, P. (2008) Multiple
988 Plagioclase Crystal Populations Identified by Crystal Size Distribution and in situ
989 Chemical Data: Implications for Timescales of Magma Chamber Processes Associated
990 with the 1915 Eruption of Lassen Peak, CA. *Journal of Petrology*, 49, 1755–1780.

- 991 Schneider, C.A., Rasband, W.S., and Eliceiri, K.W. (2012) NIH Image to ImageJ: 25 years of
992 image analysis. *Nature Methods*, 9, 671–675.
- 993 Simkin, T., and Smith, J.V. (1970) Minor-Element Distribution in Olivine. *The Journal of*
994 *Geology*, 78, 304–325.
- 995 Smith, V.G., Tiller, W.A., and Rutter, J.W. (1955) A mathematical analysis of solute
996 redistribution during solidification. *Canadian Journal of Physics*, 33, 723–745.
- 997 Soulie, C., Libourel, G., and Tissandier, L. (2017) Olivine dissolution in molten silicates: An
998 experimental study with application to condrule formation. *Meteoritics and Planetary*
999 *Science*, 52, 225–250.
- 1000 Spandler, C., and O'Neill, H.S.C. (2010) Diffusion and partition coefficients of minor and trace
1001 elements in San Carlos olivine at 1,300°C with some geochemical implications.
1002 *Contributions to Mineralogy and Petrology*, 159, 791–818.
- 1003 Thomson, A., and Maclennan, J. (2013) The Distribution of Olivine Compositions in Icelandic
1004 Basalts and Picrites. *Journal of Petrology*, 54, 745–768.
- 1005 Vinet, N., and Higgins, M.D. (2010) Magma Solidification Processes beneath Kilauea Volcano,
1006 Hawaii: a Quantitative Textural and Geochemical Study of the 1969-1974 Mauna Ulu
1007 Lavas. *Journal of Petrology*, 51, 1297–1332.
- 1008 Vinet, N., and Higgins, M.D. (2011) What can crystal size distributions and olivine compositions
1009 tell us about magma solidification processes inside Kilauea Iki lava lake, Hawaii? *Journal*
1010 *of Volcanology and Geothermal Research*, 208, 136–162.
- 1011 Vinet, N., Flemming, R.L., and Higgins, M.D. (2011) Crystal structure, mosaicity, and strain
1012 analysis of Hawaiian olivines using in situ X-ray diffraction. *American Mineralogist*, 96,
1013 486–497.

- 1014 Watson, E.B., and Liang, Y. (1995) A simple model for sector zoning in slowly grown crystals:
1015 Implications for growth rate and lattice diffusion, with emphasis on accessory minerals in
1016 crustal rocks. *American Mineralogist*, 80, 1179–1187.
- 1017 Watson, E.B., Cherniak, D.J., and Holycross, M.E. (2015) Diffusion of phosphorus in olivine
1018 and molten basalt. *American Mineralogist*, 100, 2053–2065.
- 1019 Welsch, B., Faure, F., Famin, V., Baronnet, A., and Bachelery, P. (2013) Dendritic
1020 Crystallization: A Single Process for all the Textures of Olivine in Basalts? *Journal of*
1021 *Petrology*, 54, 539–574.
- 1022 Welsch, B., Hammer, J., and Hellebrand, E. (2014) Phosphorus zoning reveals dendritic
1023 architecture of olivine. *Geology*, 42, 867–870.
- 1024 White, W.M. (1985) Sources of Oceanic Basalts: Radiogenic Isotopic Evidence. *Geology*, 13,
1025 115–118.
- 1026 White, W.M. (2010) Oceanic Island Basalts and Mantle Plumes: The Geochemical Perspective.
1027 *Annual Review of Earth and Planetary Sciences*, 38, 133–160.
- 1028 Wright, T.L. (1973) Magma Mixing as Illustrated by the 1959 Eruption, Kilauea Volcano,
1029 Hawaii. *Geological Society of America Bulletin*, 84, 849–858.
- 1030 Wright, T.L., and Klein, F. (2014) Two Hundred Years of Magma Transport and Storage at
1031 Kilauea Volcano, Hawai‘i, 1790–2008. U.S. Geological Survey Professional Paper 1806,
1032 1–258.
- 1033 Xing, C-M., Wang, C. Y., and Tan, W. (2017) Disequilibrium growth of olivine in mafic
1034 magmas revealed by phosphorus zoning patterns of olivine from mafic-ultramafic
1035 intrusions. *Earth and Planetary Science Letters*, 479, 108–199.

1036 Zhang, Y., Ni, H., and Chen, Y. (2010) Diffusion data in silicate melts. *Reviews in Mineralogy*
1037 and *Geochemistry*, 72, 311–408.

1038 Zindler, A., and Hart, S. (1986) Chemical Geodynamics. *Annual Review of Earth and Planetary*
1039 *Sciences*, 14, 493–571.

1040

1041

1042

Figure Captions

1043

Figure 1. Cross polarized photomicrographs of type 1 (**a-c**) and type 2 grains (**d**).

1044

Resorption is evident at the ends of the kink bands in grains a and b and is indicated by red

1045

arrows. White arrows indicate the locations of LA-ICP-MS transects.

1046

1047

Figure 2. Phosphorus X-ray maps of type 2 olivine, where brightness corresponds with

1048

higher P concentrations. (**a**) Resorbed olivine with P zoning that is disrupted by dissolution

1049

surfaces. (**b-d**) Olivine grains with P zoning that have equivalent Al and Cr zoning (not shown).

1050

White arrows indicate the locations of LA-ICP-MS transects, the dashed portions of the arrows

1051

show the high-P regions of the transects that were removed to compare the compositions of type

1052

1 and type 2 olivine.

1053

1054

Figure 3. Phosphorus X-ray maps of type 1 olivine. Dashed red lines indicate locations of

1055

dislocation bands. (**a**) Olivine grains with P zoning that has equivalent zoning in Al and Cr (not

1056

shown). (**b-d**) Olivine grains with P zoning only. White arrows indicate the locations of LA-ICP-

1057

MS transects, the dashed portions of the arrows show the high-P regions of the transects that

1058

were removed to compare the compositions of type 1 and type 2 olivine.

1059

1060

Figure 4. Cumulative distribution functions for select elements in olivine. Significant

1061

differences between type 1 ($n = 42$) and type 2 ($n = 42$) olivine grains are evident in slow

1062

diffusing elements Al, P, and Ti (**a-c**) No significant differences evident in the more rapidly

1063

diffusing elements, Cr (**d**), and Fe/Mg (Fo content) (**e-f**). The histogram of Fo content is shown

1064

in (**f**) for comparison with the CDF (**e**). The p-values for the two sample Kolmogorov-Smirnov

1065 test are shown, which indicates the probability that the two samples are derived from the same
1066 population. The median values of individual crystals were used to create the CDFs and
1067 histogram, when all the data are used, the CDFs are smoother and have the same general
1068 characteristics.

1069

1070 Figure 5. Kolmogorov-Smirnov test p-values plotted against the median concentration for
1071 each element in individual olivine grains. Slow diffusing elements ($< 10^{-17}$ m²/s at 1,300 °C; red
1072 symbols) that have high p-values all have low abundances in olivine (< 1 µg/g), whereas the slow
1073 diffusing elements Al, Ti, P, and V have higher abundances and lower p-values. Faster diffusing
1074 elements (blue symbols) have high p-values and high concentrations. Dashed line is $\alpha = 0.05$.

1075

1076 Figure 6. Olivine crystal size distributions for all Kilauea Iki samples. Type 1 grains have
1077 fewer small crystals and extend to larger sizes than type 2 grains. The type 1 and type 2 olivine
1078 populations also have different slopes.

1079

1080 Figure 7. Phosphorus X-ray maps of type 1 olivine showing resorption along the rims that
1081 disrupt P zoning. Red arrows indicate areas where zoning is disrupted. In areas where zoning is
1082 disrupted, there are P-poor zones between the zoning and the resorbed rim indicating some
1083 regrowth after dissolution.

1084

1085 Figure 8. Models showing the relative enrichment of the boundary layer around a crystal
1086 growing at different rates. Total crystal growth is 10 µm in each model. Each element is enriched
1087 at growth rates needed for incorporation of elevated P (Welsch et al., 2013). Element diffusion

1088 coefficients in the melt for Al and P are from Baker (2008) and Cr from Zhang et al. (2010).
1089 Partition coefficients for P, Al and Cr are from Grant and Kohn (2013), Beattie (1993) and
1090 Spandler and O'Neill (2010), respectively.

1091

1092 Figure 9. Example forward diffusion models with best-fit residence times. **(a-d)** Type 2
1093 grain (Iki-36-27-A) that has P and associated Cr zoning. **(e-h)** Type 1 grain (Iki-Scoria-14-A)
1094 that has P zoning but no associated Cr zoning. The Cr diffusion model for this grain is the
1095 minimum time necessary to erase the assumed initial Cr zoning.

1096

1097 Figure 10. Residence time estimates based on diffusion of Cr **(a)** and P **(b)** in individual
1098 olivine grains (17 profiles from 10 olivine grains). Error bars show the uncertainty in the
1099 diffusion times from the uncertainty in the diffusion coefficient and temperature estimates. The
1100 diffusion profiles that produced timescales below the shortest accurate timescales are depicted
1101 with an arrow.

1102

Table 1. Olivine textures

Sample Name	NMNH SI Catalog #	Olivine Proportion (vol %) ^a	Type 1 Olivine (vol %) ^a	Type 1/ Total Olivine (modal %) ^b	Type 1/ Total Olivine (vol %) ^a	Number of Crystals ^b	
						Type2	Type 1
All Samples		15.2	7.7	16.0	50.7	757	144
Iki-36	116111-36	14.6	6.8	13.9	46.6	196	34
Iki-43	116111-43	10.1	3.3	13.9	32.7	199	32
Iki-66	116111-66	11.7	5.6	11.5	47.9	131	17
Iki-75	116111-75	30.5	17.4	22.4	57.0	135	39
Iki-Scoria		17.6	11.7	18.6	66.5	96	22

Notes: ^a volume from 2D crystal intersections, stereologically corrected to 3D shapes (Higgins, 2006a).

^b Mode from number of crystals in the thin sections.

Table 2. Mean EBSD results for repeat spot analyses of individual grains

Crystal	Texture	n	phi1	PHI	phi2
Iki-36-1	Type 1	7	264	116	355
Iki-36-1A	Type 1	2	90	64	182
Iki-36-6	Type 2	3	115	35	348
Iki-36-6A	Type 2	2	289	147	248
Iki-36-7	Type 1	3	277	43	10
Iki-36-12	Type 2	3	237	59	70
Iki-36-25	Type 1	2	262	137	353
Iki-36-27a	Type 2	5	100	107	337
Iki-36-27b	Type 2	2	280	73	22
Iki-36-30	Type 2	6	167	92	70
Iki-36-33	Type 2	2	288	145	183
Iki-36-34	Type 2	2	118	39	350
Iki-36-35	Type 2	4	99	143	351
Iki-43-9	Type 1	4	37	40	39
Iki-43-13	Type 2	2	111	51	169
Iki-43-23	Type 1	3	7	151	338
Iki-43-25	Type 1	2	149	137	42
Iki-43-GM-2	Type 2	2	78	93	293
Iki-43-GM-3	Type 2	2	220	173	21
Iki-66-13	Type 1	3	234	166	107
Iki-66-GM-2	Type 2	5	38	47	7
Iki-66-GM-5	Type 2	2	197	55	186
Iki-Scoria-1	Type 2	2	222	172	136
Iki-Scoria-2	Type 1	3	125	102	312
Iki-Scoria-3	Type 1	3	323	142	109
Iki-Scoria-8	Type 2	3	60	119	34
Iki-Scoria-14	Type 1	3	86	100	335
Iki-Scoria-29	Type 2	3	85	76	185
Iki-Scoria-32	Type 1	2	78	95	333
Iki-Scoria-34	Type 2	2	97	82	335
Iki-Scoria-38	Type 2	3	66	126	219
Iki-Scoria-39	Type 2	3	172	141	304

1105

1106

Table 3. Minor element zoning

Olivine Texture	Imaged Grains		Grains with Zoning			Percent with Zoning		
	P and Al	Cr	P	Cr	Al	P	Cr	Al
Type 1	25	21	24	4	6	96	19	24
Type 2	44	21	39	12	16	89	57	36

1107

1108

Table 4. Two sample Kolmogorov-Smirnov test

Element	Excluding high P	Including high P
	zones p-value	zones p-value
P	0.01	<0.01
Ti	0.03	<0.01
V	0.03	<0.01
Al	<0.01	<0.01
Dy	0.35	0.57
Er	0.26	0.76
Yb	0.33	0.23
Y	0.18	0.52
Cr	0.56	0.10
Ca	0.75	0.13
Na	0.10	0.16
Co	0.56	0.62
Sc	0.91	0.41
Ni	0.26	0.48
Fe	0.56	0.55
Mg	0.39	0.71
Mn	0.91	0.63
Li	0.40	0.98

Note: Elements listed in approximate order of increasing diffusivity.

1109

1110

1111

Table 5. CSD Results

	CSD Slope	Intercept	Goodness of Fit (Q)
Type 1	-1.23 (0.08)	-1.81 (0.32)	0.46
Type 2	-2.87 (0.10)	1.52 (0.14)	7.5×10^{-5}
V&H G2a	-2.7	1.3	
V&H G2b	-1.11	-2.28	
Mangan	-2.88	1.03	

Note: Values in parenthesis are 1 s uncertainties
V&H: Vinet and Higgins (2011), Mangan: Mangan (1991)

1112

1113

1114

Table 6. Equilibrium liquid temperature estimates

	$K_D = 0.28$		$K_D = 0.30$		$K_D = 0.33$		$K_D = 0.34$	
	Average T (°C)	Standard deviation						
All	1234	21	1195	22	1214	23	1220	23
Type 1	1233	21	1194	22	1213	23	1219	24
Type 2	1236	21	1197	21	1216	23	1222	23

1115

1116

Table 7. Results of diffusion modeling

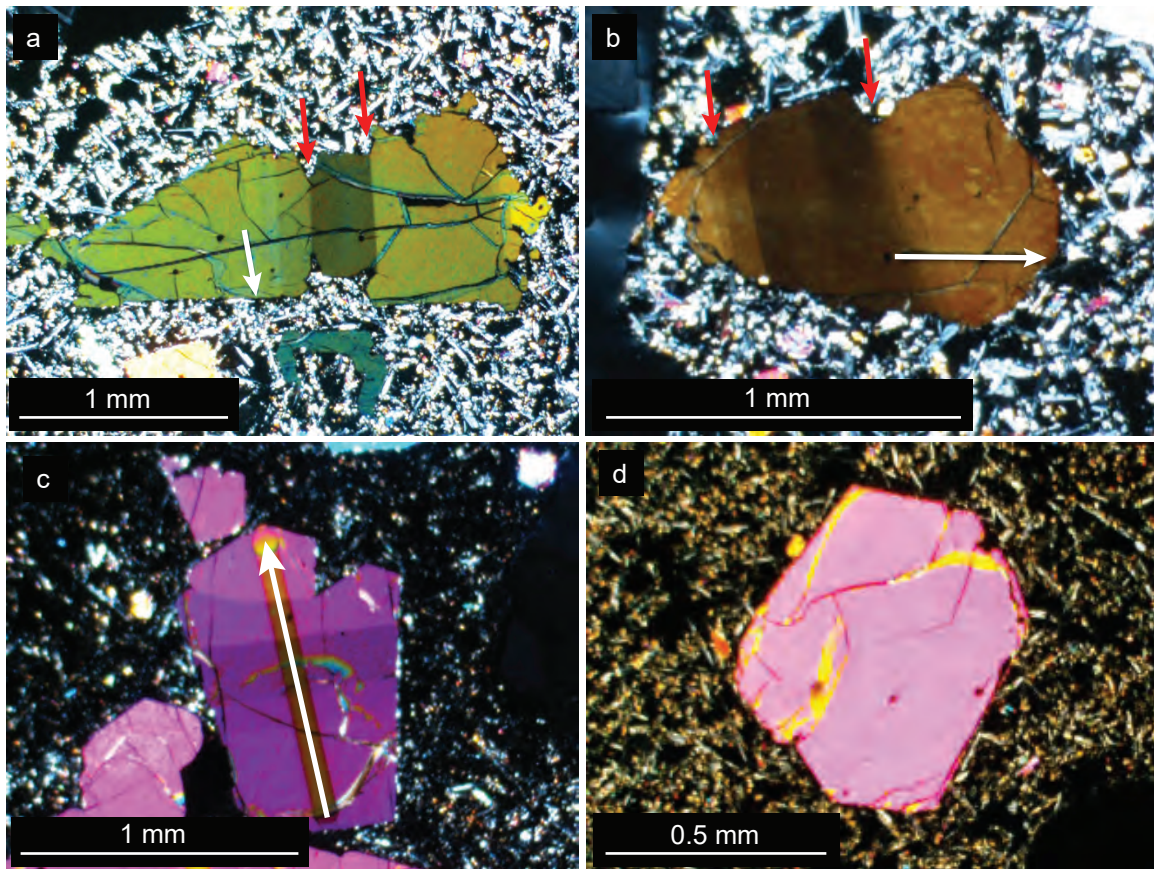
Sample	Cr diffusion time (days)	P diffusion time (days)	Comments	Orientation ^a		
				α	β	γ
Type 2						
Iki-36-27-A	22	< 46		56	119	58
Iki-36-27-C	82	127		96	69	158
Iki-36-30-C	< 5	84		119	21	83
Iki-43-GM-2b-A	4	< 22		109	47	49
Iki-66-GM-2b-D	< 2	< 22		19	116	81
Iki-66-GM-5b-B	5	< 22		75	57	143
Iki-66-GM-5b-C	35	< 22		98	55	143
Iki-Scoria-1-C	5	< 43		86	173	85
Type 1						
Iki-43-23-A	2665	238	No Cr zoning	179	83	82
Iki-43-25-A	2279	< 33	No Cr zoning	71	49	133
Iki-43-25-B	1111	34	No Cr zoning	112	31	111
Iki-66-13-A	10	< 53		81	171	88
Iki-Scoria-14-A	3932	< 72	No Cr zoning	113	73	151
Iki-Scoria-14-D	3747	< 72	No Cr zoning	33	109	127
Iki-Scoria-14-E	1591	71	No Cr zoning	41	117	61
Iki-Scoria-2-B	15746	200	No Cr zoning	53	118	130
Iki-Scoria-2-C	1967	113	No Cr zoning	75	89	165

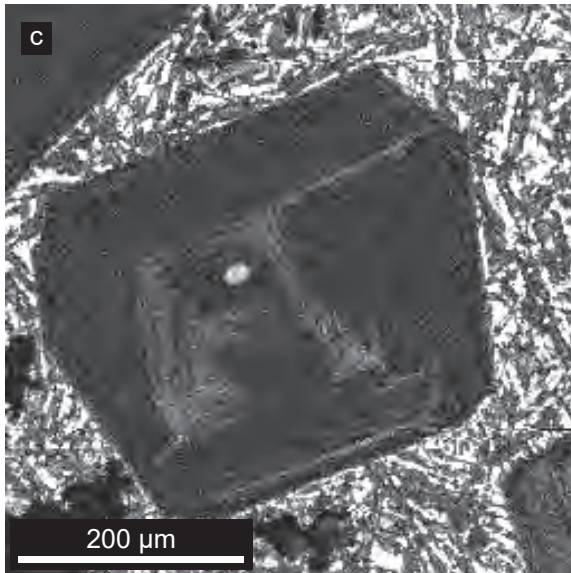
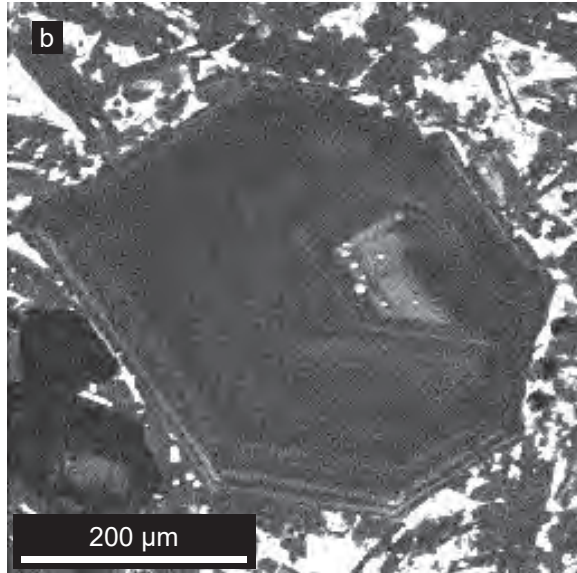
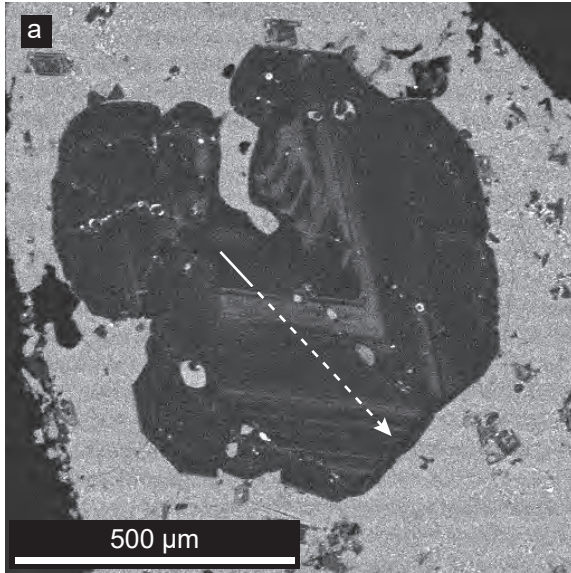
Note: ^a α , β , and γ are the angles between the measured transect and the a, b, and c axes, respectively

1117

1118

Figure 1.





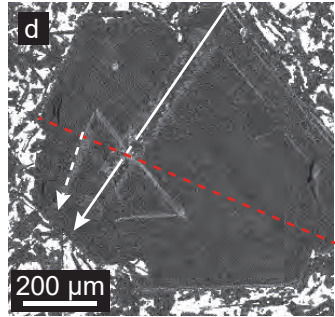
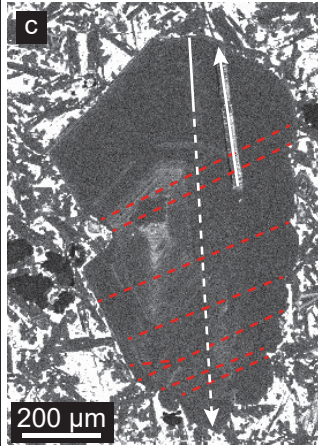
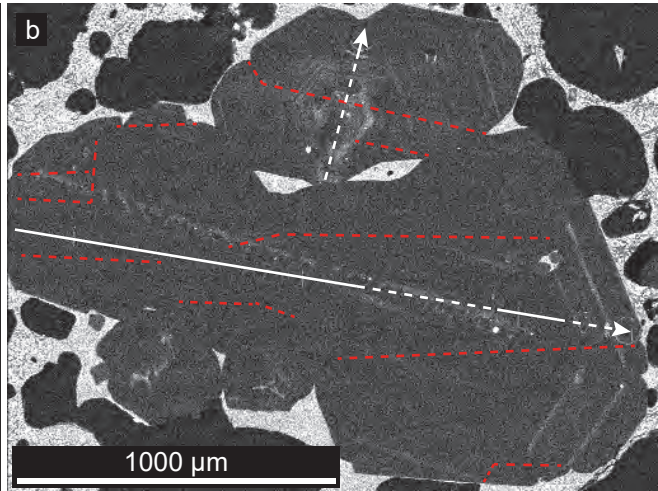
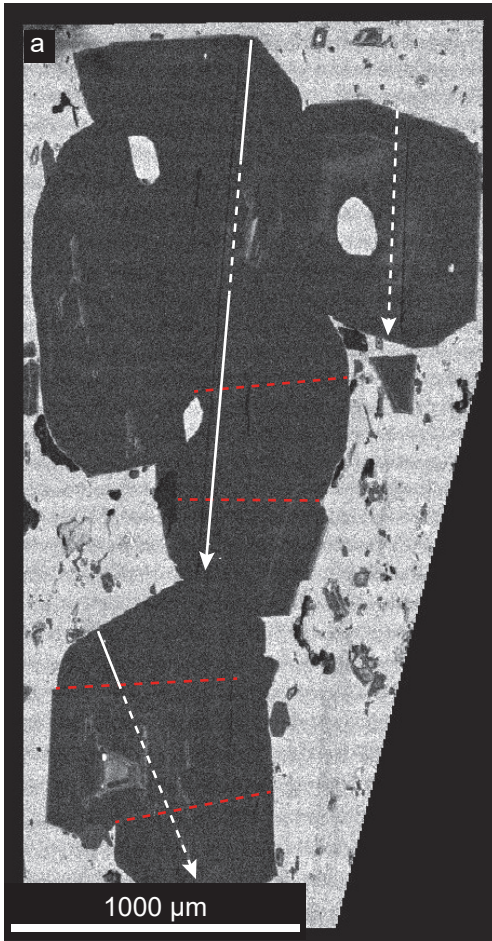


Figure 4

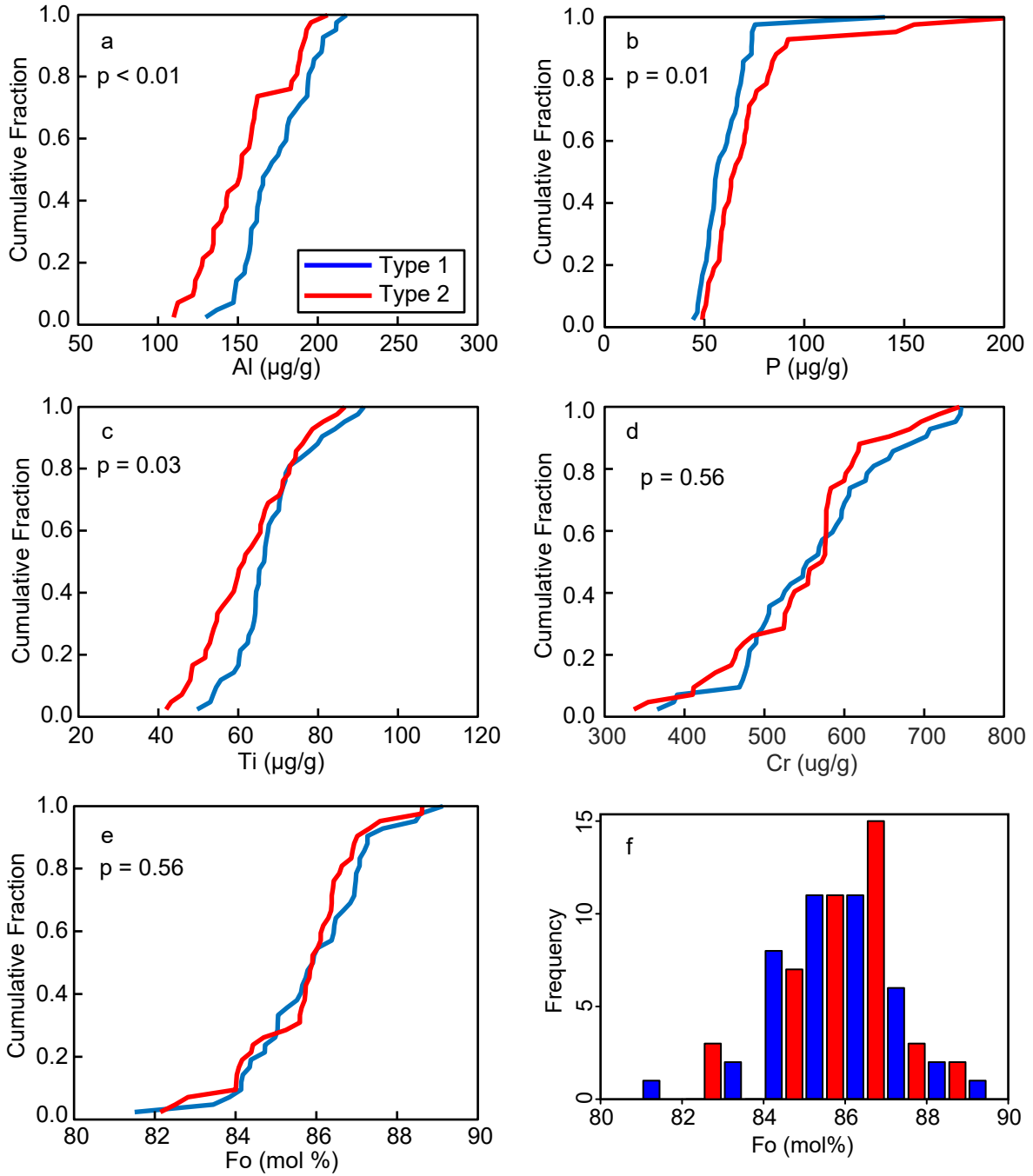


Figure 5

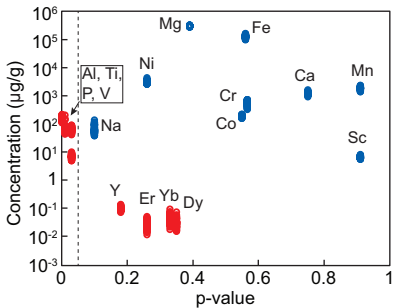


Figure 6

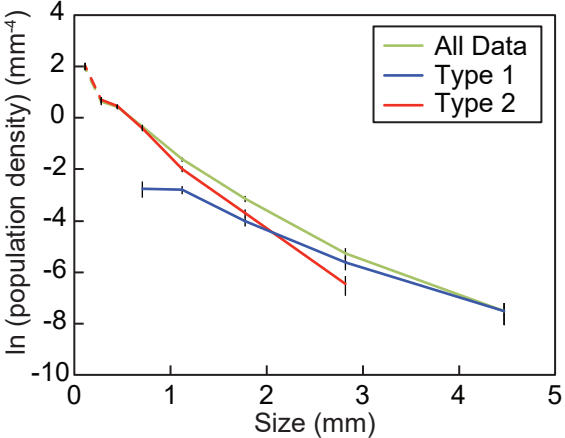


Figure 7

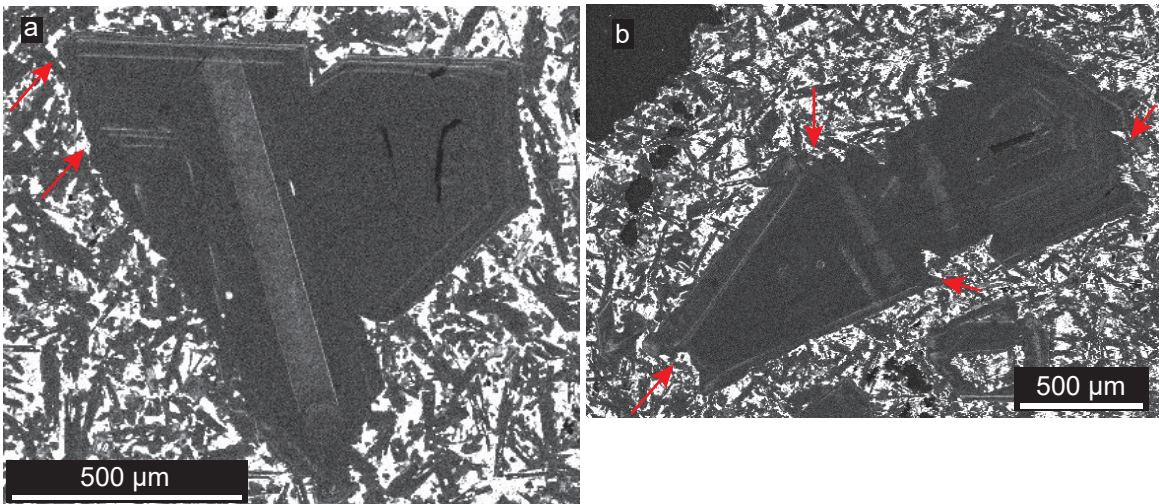


Figure 8

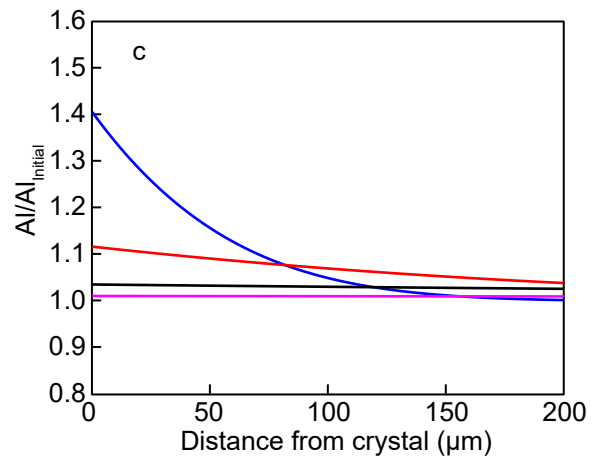
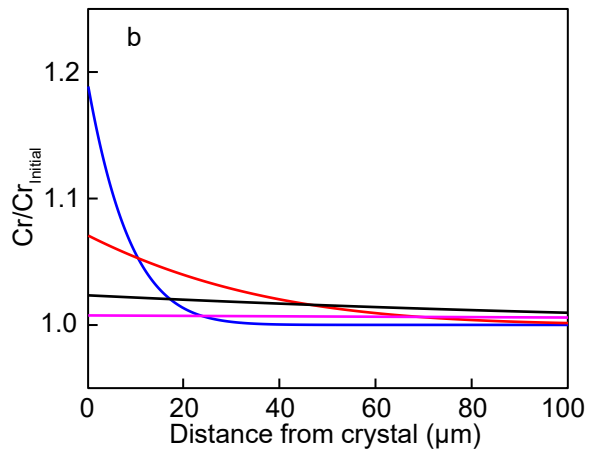
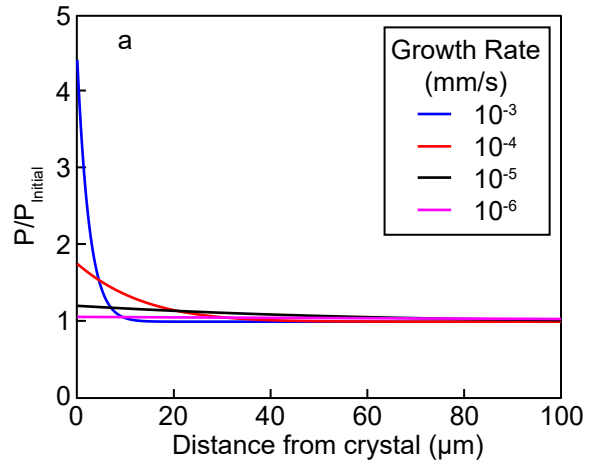


Figure 9

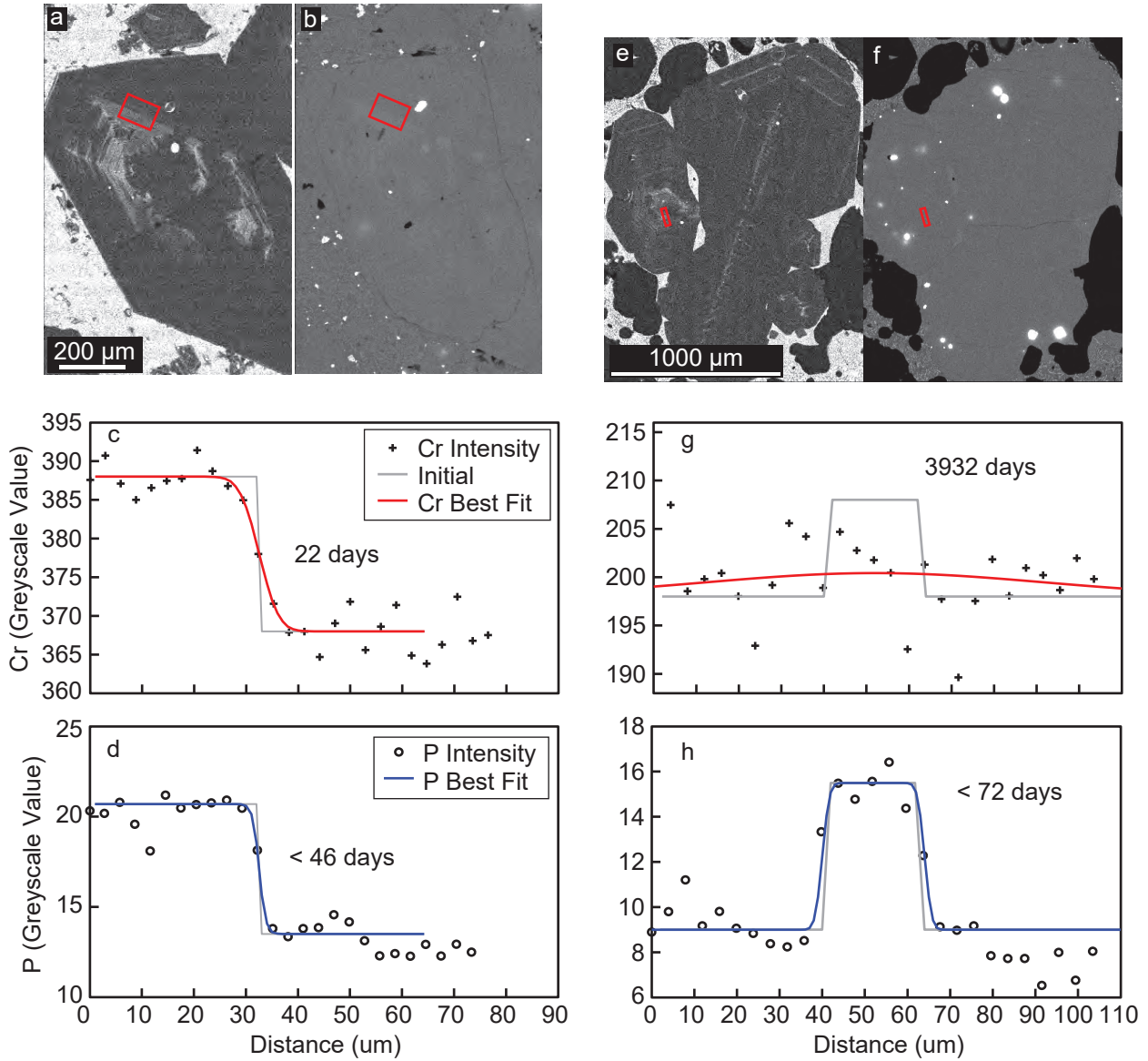


Figure 10

